

An empirical model of tropical ocean dynamics

Matthew Newman¹, Michael A. Alexander², and James D. Scott¹

¹CIRES Climate Diagnostics Center, University of Colorado, and Physical Sciences Division/NOAA Earth System Research Laboratory, Boulder, Colorado

²Physical Sciences Division/NOAA Earth System Research Laboratory, Boulder, Colorado

Email: matt.newman@noaa.gov

Submitted to *Climate Dynamics* Wednesday, April 7, 2010

ABSTRACT

To extend the linear stochastically forced paradigm of tropical sea surface temperature (SST) variability to the subsurface ocean, a linear inverse model (LIM) is constructed from the simultaneous and 3-month lag covariances of observed 3-month running mean anomalies of SST, thermocline depth, and zonal wind stress. The impact of the additional variables on LIM SST forecasts is small for short leads but enhances forecasts at longer leads. For example, Nino3.4 forecast skill remains above 0.6 at 14-month lead. Similarly, the extended LIM predicts lag covariances and associated power spectra whose close agreement with observations, particularly on longer time scales, additionally validates the linear model.

The extended LIM also enables comparison between empirically-determined linear dynamics and ENSO physical mechanisms. Optimal growth of SST anomalies over several months is now clearly related to an initial central equatorial Pacific thermocline anomaly, which propagates eastward and leads the amplifying SST anomaly. The initial SST and thermocline anomalies each result in roughly half the SST amplification. Optimal growth occurs as two stable eigenmodes with similar structure but differing 2- and 4-year periods evolve from initial destructive to weakly constructive interference. These eigenmodes provide compact representation of mixed SST/ocean ENSO dynamics so their coupled GCM counterparts could serve as an ENSO metric.

For time intervals beyond 9 months, a secondary type of optimal growth exists in which initial SST anomalies in the southwest tropical Pacific and Indian ocean play a larger role, apparently driving sustained off-equatorial wind stress anomalies in the eastern

Pacific that result in a more persistent equatorial thermocline anomaly and a more protracted (and predictable) ENSO event.

1 Introduction

Penland and Sardeshmukh (1995; hereafter PS95) showed that observed tropical SST variability may be viewed as the linear stochastically-forced system

$$(1) \quad \frac{d\mathbf{T}_o}{dt} = \mathbf{L}\mathbf{T}_o + \mathbf{F}_s ,$$

where $\mathbf{T}_o(t)$ are sea surface temperature (SST) anomalies throughout the tropical domain, \mathbf{L} is a stable linear dynamical operator, and \mathbf{F}_s is white noise (which has spatial coherence). PS95 derived \mathbf{L} empirically by constructing a Linear Inverse Model (LIM); a similar result has also been suggested by several studies using intermediate coupled models (Flügel and Chang 1996; Moore and Kleeman 1997, 1999; Penland et al. 2000; Thompson and Battisti 2001). Eq. (1) may be thought of as a multivariate extension to the univariate red noise null hypothesis for SST variability first proposed by Frankignoul and Hasselman (1977), in which the slowly evolving ocean integrates forcing by rapidly evolving weather noise. The “effectively linear” stochastic approximation (1) is similarly valid when nonlinear processes decorrelate much more rapidly than linear processes (e.g., Papanicolaou and Kohler 1974; Hasselmann 1976; see also Penland 1996), so that nonlinear terms may be parameterized as a (second) linear process plus unpredictable white noise. [This is in contrast to “linearization” of the prevailing equations, where it is assumed that the magnitude, rather than the time scale, of the nonlinear terms is small.]

Eq. (1) is a very good approximation of the observed statistics of ENSO evolution. For example, a LIM constructed from the zero- and one week lagged covariance statistics of

weekly atmospheric and SST data more faithfully reproduces the entire power spectrum on seasonal to interannual time scales of the leading EOF of monthly tropical SST variability than do the corresponding spectra from virtually all ensemble members of the “20th-century” (20c3m) IPCC AR4 coupled GCMs (Newman et al. 2009). Also, forecasts made using the LIM are not only competitive with operational GCMs such as NCEP’s coupled forecast system (CFS) but, particularly for forecast leads of six months and greater, generally have higher skill throughout most of the Pacific Basin (not shown), indicating that (1) is also a good approximation of the case-to-case evolution of SST anomalies.

While (1) has proven highly useful as a dynamical model for SSTs, it is not entirely satisfactory as a dynamical model of the full ocean. Eq. (1) assumes that SST is a proxy for the complete coupled atmosphere-ocean state vector, which PS95 notes is a plausible scenario so long as essentially instantaneous (on the seasonal time scale) SST-induced changes in surface winds drive an immediate thermocline response, and/or in the fast-wave limit (Neelin 1991; Neelin and Jin 1993) in which wave dynamics allow the deeper ocean to rapidly adjust to changes in SSTs. In this case, all other physically important ocean variables can be effectively regressed onto SST; that is, $\mathbf{X} = \mathbf{B} \mathbf{T}_o + \mathbf{r}$, where \mathbf{X} is the remaining ocean state vector, \mathbf{B} is a regression matrix and \mathbf{r} is a white residual. (Note that this regression is generally not local.) Consequently, \mathbf{L} in (1) includes all the *implicit* effects of \mathbf{X} upon the evolution of \mathbf{T}_o . Clearly, this is at least partly true, evidenced both by a strong observed relationship between thermocline depth and SST (e.g., Zelle et al. 2004) and by the success of (1) as a model.

However, for longer time scales (and thus forecast leads) we expect that deeper ocean physics will become too important for this simple relationship to hold, if for no other reason than \mathbf{r} is unlikely to be white. For example, near-equatorial Kelvin and Rossby waves are an integral part of the El Niño phenomena, and within the delayed oscillator paradigm the latter set the time scale for ENSO (Schopf and Suarez 1988; Battisti and Hirst 1989). In the subtropics, thermocline variability clearly propagates west in accordance with Rossby wave theory and appears to influence the upper ocean along the equator via Kelvin waves along the western boundary (Capotondi and Alexander 2001). In the recharge-discharge paradigm for ENSO, zonally-averaged export of heat to and from the equator is the critical process for ENSO dynamics (Jin 1997). Indeed, heat content anomalies at 5°N, important in either paradigm, contribute to ENSO predictability at 6 to 12 month lead times (Latif and Graham 1992).

Moreover, we wish to understand why the LIM serves to answer this question: what dynamical system results from the interaction of known (and unknown) atmospheric and oceanic processes in the Tropics? To diagnose coupled air-sea processes, a LIM based on SST alone is necessarily insufficient, so both atmospheric and subsurface information must be included in the model state vector. As a first step, in this study we have extended the LIM to include thermocline depth (as represented by the 20°C isotherm depth) and surface zonal wind stress. The extended LIM, described in section 2, improves both tropical SST predictions at longer leads and the simulation of power spectra and lag covariance statistics relative to the SST-only LIM, as shown in section 3. Some analysis of the different terms within the LIM and their effect upon SST variations is made in section 4. A discussion of how inclusion of thermocline depth impacts the most rapidly

amplifying SST anomalies and how they evolve into ENSO events is presented in section 5, along with how key eigenmodes of \mathbf{L} contribute to this evolution. Concluding remarks are made in section 6.

2 Model details and data

LIM may be broadly defined as extracting the dynamical evolution operator of the system

$$(2) \quad \frac{d\mathbf{x}}{dt} = \mathbf{L}\mathbf{x} + \xi,$$

from its observed statistics, as described for example in PS95 (see also Penland 1989, 1996; Winkler et al 2001; Newman et al 2003; Newman 2007; Alexander et al. 2008; Newman and Sardeshmukh 2008; Newman et al. 2009). The procedure and its strengths and pitfalls are discussed at length in these papers, so we will only provide its bare essentials here.

In any multidimensional statistically stationary system with components x_i , one may define a time lag covariance matrix $\mathbf{C}(\tau)$ with elements $C_{ij}(\tau) = \langle x_i(t+\tau)x_j(t) \rangle$, where angle brackets denote a long term average. In linear inverse modeling, one assumes that the system satisfies $\mathbf{C}(\tau) = \mathbf{G}(\tau)\mathbf{C}(0)$, where importantly $\mathbf{G}(\tau) = \exp(\mathbf{L}\tau)$ and \mathbf{L} is a constant matrix, which follows from (2). One then uses this relationship to estimate \mathbf{L} from observational estimates of $\mathbf{C}(0)$ and $\mathbf{C}(\tau_0)$ at some lag τ_0 . In such a system any two states separated by a time interval τ are related as $\mathbf{x}(t+\tau) = \mathbf{G}(\tau)\mathbf{x}(t) + \epsilon$, where ϵ is a random error vector with covariance $\mathbf{E}(\tau) = \mathbf{C}(0) - \mathbf{G}(\tau)\mathbf{C}(0)\mathbf{G}^T(\tau)$. Note that the system need not have Gaussian statistics for these relations to hold. However, for its statistics to be stationary, \mathbf{L} must be dissipative, i.e its eigenvalues must have negative real parts. In a

forecasting context, $\mathbf{G}(\tau)\mathbf{x}(t)$ represents the “best” forecast (in a least squares sense) of $\mathbf{x}(t+\tau)$ given $\mathbf{x}(t)$, and $\mathbf{E}(\tau)$ represents the expected covariance of its error. For large lead times τ , $\mathbf{G}(\tau)\mathbf{x}(t) \Rightarrow 0$ and $\mathbf{E}(\tau) \Rightarrow \mathbf{C}(0)$. Note that unlike multiple linear regression, determination of \mathbf{G} at one lag τ_0 identically gives \mathbf{G} at all other lags. Also, statistics of the noise forcing, not just the error covariance, are determined by LIM since the positive-definite noise covariance matrix $\mathbf{Q} = \langle \xi \xi^T \rangle dt$ is determined from a Fluctuation-Dissipation relationship,

$$(3) \quad d\mathbf{C}(0)/dt = \mathbf{0} = \mathbf{L}\mathbf{C}(0) + \mathbf{C}(0)\mathbf{L}^T + \mathbf{Q} ,$$

given the observed $\mathbf{C}(0)$ and \mathbf{L} .

For the LIM presented in this paper, we chose the model state vector \mathbf{x}

$$\mathbf{x} = \begin{bmatrix} \mathbf{T}_O \\ \mathbf{Z}_{20} \\ \tau_x \end{bmatrix}$$

where \mathbf{T}_O is anomalous SST, \mathbf{Z}_{20} is anomalous 20⁰C isotherm depth, and τ_x is anomalous surface zonal wind stress. Forty-two years (1959 to 2000) of 3-month running mean data were used to define \mathbf{x} . Monthly means of \mathbf{T}_O and \mathbf{Z}_{20} can also be used to construct LIMs, but this time scale is problematic when an atmospheric variable is included because of some aliasing of the Madden-Julian oscillation (MJO) signal. SST data were obtained from the Hadley Sea Ice and Sea Surface Temperature analysis (HadISST; Rayner et al. 2003), 20⁰C isotherm depth was determined from the SODA dataset (Carton and Giese 2008), and wind stress from the NCEP Reanalysis (Kalnay et al. 1996). The data were

averaged into 2° latitude x 5° longitude gridboxes. Anomalies were then determined by removing the long-term monthly mean.

Anomalies were projected onto their leading Empirical Orthogonal Functions (EOFs) determined for the region 25°S — 25°N . Prior to computing EOFs, each field was normalized by its domain-averaged climatological root-mean-square amplitude. The leading 13/7/3 EOFs of $\mathbf{T}_o/\mathbf{Z}_{20}/\tau_x$ were retained, which explained about 83/36/32 percent of the variability of their respective fields. Locally, however, variance explained can be considerably higher (or lower), as seen in Fig. 1, which shows the (untruncated) variance of \mathbf{T}_o , \mathbf{Z}_{20} , and τ_x , and the local fraction of variance explained by the truncated EOF basis for each field.

The time-varying coefficients of these EOFs, i.e., the principal components (PCs), define the 23-component state vector \mathbf{x} . A training lag of $\tau_o=3$ months was used to determine \mathbf{L} . The EOF truncations and training lag were chosen to maximize the LIM's cross-validated forecast skill for leads up to 18 months, while avoiding the Nyquist problem for \mathbf{L} (PS95) that inhibits analysis of interactions amongst the model variables. In no other respect do our choices of training lag and EOF truncation for any variable qualitatively affect the points made in this paper. For purposes of comparison, we also constructed corresponding LIMs (SST13-LIM and SST23-LIM) using either a 13- or 23-component \mathbf{T}_o state vector to represent \mathbf{x} alone.

Finally, the LIM must be tested on data independent of that used to determine \mathbf{L} . Estimates of \mathbf{L} and of forecast skill were cross-validated as follows. We sub-sampled the data record by sequentially removing one five-year period, computed \mathbf{L} for the remaining

years, and then generated forecasts for the independent years. This procedure was repeated for the entire period. Forecast skill in this study is based upon these jack-knifed forecasts, determined by comparing the local anomaly correlation between the cross-validated model predictions and gridded *untruncated* verifications.

3 Evaluating the LIM

3.1 Forecast skill

Explicitly including both τ_x and \mathbf{Z}_{20} in the LIM state vector increases skill of 9 (Figs. 2a and b) and 18 (Figs. 2c and d) month \mathbf{T}_o forecasts. Skill improvement is mostly due to the inclusion of \mathbf{Z}_{20} rather than τ_x , confirming that the \mathbf{Z}_{20} data provides useful information. In addition, the LIM makes \mathbf{Z}_{20} forecasts. Earlier studies (e.g., PS95) found that LIM SST forecast skill is much better than persistence, and we find this is also true of \mathbf{Z}_{20} LIM skill (not shown). The difference in SST skill between the extended and SST-LIMs generally increases with forecast lead because the extended LIM captures the slower \mathbf{Z}_{20} evolution. For example, a second set of “fixed- \mathbf{Z}_{20} ” extended LIM forecasts in which the initial \mathbf{Z}_{20} anomaly is persisted through the forecast period (i.e., $\mathbf{Z}_{20}(t) = \mathbf{Z}_{20}(0)$; not shown) has greatly reduced 18-month forecast skill.

Figure 3 shows that the extended LIM improves Niño 3.4 \mathbf{T}_o forecast skill for all forecast leads. A few previous linear empirical model studies also included some variable related to subsurface variability (Johnson et al. 2000; Xue et al. 2000), finding similar skill improvement. On the other hand, for leads up to about 8 months the SST23-LIM, with the same number of degrees of freedom, has about the same skill as the extended LIM. That is, replacing higher order SST PCs with subsurface information in the LIM does not

notably improve skill for shorter leads, a result earlier noted by C. Penland (personal communication) and Johnson et al. (2000). For longer leads, however, the extended LIM has higher skill than SST-LIMs of any EOF truncation. [In fact, for forecast leads over one year, SST-LIM skill is degraded when using more than 13 EOFs.] As a result, if we define a “good” forecast as having anomaly correlation skill greater than or equal to 0.6, then the extended LIM improves Niño 3.4 forecast skill by about 3-4 months. A similar result also obtains over the Indian Ocean (not shown).

3.2 *Observed and LIM lag-covariability*

Having constructed the LIM, we must also test the validity of the linear approximation through a “tau-test” (PS95). For example, since (2) implies that $\mathbf{C}(\tau) = \mathbf{G}(\tau) \mathbf{C}(0)$, the LIM should be able to reproduce observed lag-covariance statistics at much longer lags than the 3 month lag on which the LIM was trained (e.g., $\mathbf{C}(18) = [\mathbf{G}(3)]^6 \mathbf{C}(0)$).

Figure 4 compares the observed and predicted lag-autocovariances of \mathbf{T}_O for lags of 9, 18, and 36 months, using both the extended LIM and the SST13-LIM. The SST13-LIM does a reasonably good job capturing the main aspects of the lag-autocovariance pattern, but for lags less than about a year it tends to overestimate persistence especially along the equator. For longer lags, the SST13-LIM captures the sign change to negative lag-autocovariance but tends to underestimate its amplitude and does not return to positive values for lags over three years. The extended LIM improves upon these deficiencies, as well as reproducing observed lag-covariance for \mathbf{Z}_{20} over the same lags (not shown).

3.3 Power spectra

A complementary test of linearity more directly compares the LIM's predicted low-frequency variance with observations by either computing power in desired frequency bands directly from (2) as in Penland and Ghil (1993), or by making a long run of (2) and collecting statistics. We followed the latter approach, integrating (2) for 42000 years using the method described in Penland and Matrosova (1994). The white noise forcing $\xi = \sum_j \mathbf{q}_j \eta_j r_j(t)$ was specified using independent Gaussian white noises $r_j(t)$ with unit variance, where \mathbf{q}_j and $(\eta_j)^2$ as the eigenvectors and eigenvalues, respectively, of the positive-definite noise covariance matrix \mathbf{Q} determined as a residual from (3). This solution is guaranteed to be symmetric but not positive-definite. Indeed we found one small negative eigenvalue of \mathbf{Q} accounting for less than 0.25% of the trace of \mathbf{Q} . Following Penland and Matrosova (1994), we produced a legitimate modified noise covariance matrix by setting this negative eigenvalue to zero, rescaling the remaining positive eigenvalues to preserve the total forcing variance, and reconstructing \mathbf{Q} using the rescaled eigenvalues and corresponding eigenvectors. Finally, a modified $\mathbf{C}(0)$ consistent with (2) was recalculated from (3) by specifying \mathbf{L} and the modified \mathbf{Q} . The impact of this modification upon the modified $\mathbf{C}(0)$ was almost negligible.

The resulting model “data” is separated into 1000 42-yr time series. The observed spectra and the ensemble mean of the model spectra for the three leading PCs of \mathbf{T}_O and \mathbf{Z}_{20} are shown in Figs. 5 and 6, respectively. The corresponding EOF pattern for each spectrum is shown in the inset panels. The gray shading shows the 95% confidence intervals of these spectra, estimated using the 1000 model realizations.

The LIM reproduces the main features of the observed power spectra for the leading PCs of each variable (including τ_x , not shown). Obviously, the mean LIM spectra are much smoother than observed, due to the relatively few degrees of freedom in the truncated EOF space. On the other hand, the irregularity of the observed spectra is at least partly due to sampling, as indicated by the confidence intervals, which show how much variation in the spectra could occur simply from different realizations of noise.

4 Processes within the dynamical operator

The dynamics of different tropical oceanic processes may be investigated by rewriting (2) as

$$(4) \quad \frac{d}{dt} \begin{bmatrix} \mathbf{T}_O \\ \mathbf{Z}_{20} \\ \boldsymbol{\tau}_x \end{bmatrix} = \begin{bmatrix} \mathbf{L}_{TT} & \mathbf{L}_{TZ} & \mathbf{L}_{T\tau} \\ \mathbf{L}_{ZT} & \mathbf{L}_{ZZ} & \mathbf{L}_{Z\tau} \\ \mathbf{L}_{\tau T} & \mathbf{L}_{\tau Z} & \mathbf{L}_{\tau\tau} \end{bmatrix} \begin{bmatrix} \mathbf{T}_O \\ \mathbf{Z}_{20} \\ \boldsymbol{\tau}_x \end{bmatrix} + \begin{bmatrix} \xi_T \\ \xi_Z \\ \xi_\tau \end{bmatrix}.$$

Note that \mathbf{L}_{TT} is distinct from the SST-LIM linear operator, which implicitly includes linear diagnostic relationships between \mathbf{Z}_{20} and $\boldsymbol{\tau}_x$ and \mathbf{T}_O . By explicitly separating out the effects of the other two variables on \mathbf{T}_O and vice versa, we can use (4) to identify \mathbf{L}_{TT} with surface ocean processes, \mathbf{L}_{ZZ} with internal ocean processes, $\mathbf{L}_{\tau\tau}$ with surface atmospheric processes, and the off-diagonal submatrices with coupling. Of course, these operators each implicitly retain the influence of variables not included in \mathbf{x} , especially considering the more severe EOF truncation of \mathbf{Z}_{20} and $\boldsymbol{\tau}_x$, and to the extent that the terms are related to the *same* unspecified variables they may not be entirely independent.

With this important caveat in mind, we “remove” the effects of thermocline variability by using a new operator \mathbf{L}_{noz} , where we set $\mathbf{L}_{ZT} = \mathbf{L}_{TZ} = \mathbf{L}_{\tau Z} = \mathbf{L}_{Z\tau} = 0$ in \mathbf{L} , to make a second

42000 yr run. The resulting SST PC spectra (green lines in Figs. 5 and 6) are all more sharply peaked with decadal variability significantly reduced. Moreover, variability of $T_O/PC3$ is sharply increased and dominates $T_O/PC1$ and $T_O/PC2$ on decadal time scales. Overall, uncoupling weakly increases equatorial T_O variance in the central Pacific Niño4 region but strongly decreases it, by about one third, in the eastern Pacific Niño3 region (not shown).

The covariance budget of 3-month running mean SST anomalies, derived from (3) and (4) as

$$(5) \quad [\mathbf{L}_{TT}\mathbf{C}_{TT} + \mathbf{C}_{TT}\mathbf{L}_{TT}^T] + [\mathbf{L}_{TZ}\mathbf{C}_{ZI} + \mathbf{C}_{TZ}\mathbf{L}_{TZ}^T] + [\mathbf{L}_{T\tau}\mathbf{C}_{\tau T} + \mathbf{C}_{T\tau}\mathbf{L}_{T\tau}^T] + \mathbf{Q}_{TT} = \mathbf{O},$$

SST Thermocline interaction Wind stress Stochastic

where $\mathbf{C}_{xy} = \langle \mathbf{xy}^T \rangle$, is another gauge of anomalous thermocline and wind stress influences on SST variability. The diagonal elements in each bracketed term in (5) may be interpreted as their contribution to the local T_O variance tendency. Note that although these terms relate to the maintenance of local variance, they contain non-local effects: \mathbf{L}_{TT} and \mathbf{C}_{TT} are not diagonal matrices, and thermocline and zonal wind stress variability contribute to SST variability. In principle this “inverse” method of determining the interannual heat budget should agree with a more traditional “forward” approach in which all terms in the surface-layer heat budget are explicitly calculated (e.g., Wang and McPhaden 2000).

It is interesting to break down the bracketed SST term further into “local” (Fig. 7a) and “non-local” (Fig. 7b) contributions. The local contribution, twice the product of the

diagonal elements of \mathbf{L}_{TT} with the corresponding diagonal elements of \mathbf{C}_{TT} , results in a dissipative term of the form $-2\langle(T_O)^2\rangle/\tau_d$ (where τ_d is a local decay time scale) with stronger damping in the eastern and equatorial central Pacific ($\tau_d \sim 6-7$ months) than in the western and subtropical central Pacific ($\tau_d \sim 10-15$ months). Note that this regional variation of damping includes effects both of local SST-related variations of radiative and surface heat fluxes (e.g., Kessler and McPhaden 1995; Wang and McPhaden 2000) and of vertical mixing related to stronger mean upwelling in the east. The non-local term is the difference between the total term (not shown) and the local term, representing how all other values of T_O impact local T_O variability, such as through advection and/or wave propagation. This term also generally acts to damp equatorial SST variance as might be expected from the mean advection of thermal anomalies (Jin et al 2006) and meridional transport due to tropical instability waves (Wang and McPhaden 2000; Jochum et al. 2007), except in the central Pacific and around $5-10^\circ\text{N}$ where it acts to generate SST variance, consistent with the downgradient transport of SST variance (cf. Fig. 1) by high frequency eddy fluxes (Wang and McPhaden 2000) and mean equatorial zonal and off-equatorial meridional currents (Kang et al 2001).

The primary balance in Fig. 7 is between thermocline interactions (Fig. 7c) and the SST dynamical terms. The thermocline term, which is positive except in the central Pacific, includes the net SST variance generation by local thermocline and upwelling feedbacks, and also non-local zonal advective feedback (Picaut et al. 1996; Jin and An 1999) due to the dependence of anomalous zonal current on the anomalous equatorial thermocline gradient. T_O noise effects are very small (Fig. 7e) except in a narrow equatorial band where tropical instability waves are active (Chelton et al. 2000); in fact, atmospheric

noise forcing has a greater but indirect effect upon SSTs primarily by maintaining zonal wind stress variability (not shown), which in turn forces thermocline variability. While there is a weaker direct zonal wind stress forcing term (Fig. 7d), it might also implicitly represent other anomalous surface wind effects on latent and sensible heat fluxes, and even radiative fluxes due to cloudiness. Note that advective feedbacks in the central Pacific appear to mostly be contained within the thermocline term and do not represent direct effects from the wind stress forcing term as in the “wind stress feedback” (Burgers and van Oldenborgh 2003).

5 Optimal evolution of ENSO

5.1 *Maximum amplification of SST anomalies in SST- and extended LIMs*

PS95 showed that the “optimal” initial condition for maximum amplification of tropical SST anomalies, obtained via a singular vector decomposition (SVD) of the system propagator $\mathbf{G}(\tau)$ under the L2 norm (i.e., domain-mean square amplitude) of \mathbf{T}_O (e.g., Farrell 1988; PS95), is also the most relevant initial condition for ENSO development. The SVD analysis yields a dominant pair $\mathbf{u}_1, \mathbf{v}_1$ of normalized singular vectors and maximum singular value λ_1 , such that the initial condition \mathbf{v}_1 leads to the anomaly $\mathbf{G} \mathbf{v}_1 = \lambda_1 \mathbf{u}_1$ at time $t = \tau$. The maximum possible anomaly growth factor $\lambda_1^2(\tau)$, sometimes called a “maximum amplification” (MA) curve (PS95), is displayed in Fig. 8a for each LIM. For consistent comparison, the L2 norm is defined in the space of the leading 13 EOFs of \mathbf{T}_O in all three cases.

The shape and maximum (at $\tau \sim 8$ -9 months) of the MA curve for each SST-LIM is consistent with earlier studies including PS95. Although in principle an optimal initial

condition for one value of τ does not have to be optimal for another value of τ , in reality PS95 found relatively little difference in the leading optimal structure for a wide range of τ . This result is also true for our SST-LIMs; for example the pattern correlation of $\mathbf{v}_1(9 \text{ months})$ with $\mathbf{v}_1(\tau)$ is greater than 0.9 for τ ranging from about 4 to 14 months (Fig. 8b). That is, for all practical purposes the SST-LIM has only one leading optimal initial structure.

The shape of the MA curve for the extended LIM is quite different, however, with a secondary maximum at $\tau \sim 17\text{-}18$ months and a fairly flat curve between the two maxima. Moreover, these two maxima represent somewhat different optimal structures, with an 0.35 pattern correlation between $\mathbf{v}_1(9 \text{ months})$ and $\mathbf{v}_1(18 \text{ months})$ (Fig. 8b). However, although the initial states are different, the end results are similar, with both optimal initial conditions evolving into a large central and eastern Pacific SST anomaly (see below discussion). The increased maximum amplification for the extended LIM implies increased predictability (Newman et al. 2003) for forecast leads greater than about nine months, which appears realized in the forecasts described in section 3.

5.2 *Evolution of 9- and 18-month leading optimal structures*

To explore the differences between these two leading optimal structures, we integrate (2) forwards from either initial condition $\mathbf{v}_1(9)$, the optimal structure for growth over a $\tau = 9$ month interval (Fig. 9a), or from initial condition $\mathbf{v}_1(18)$, the optimal structure for growth over a $\tau = 18$ month interval (Fig. 10a). For ease of comparison, both initial conditions are chosen with sign leading to a warm event, but in this linear model all signs can be flipped. The evolution from $\mathbf{v}_1(9)$ [$\mathbf{v}_1(18)$] over the next 36 months is displayed in Figs.

9b-d [10b-d]. Forcing by \mathbf{Z}_{20} (τ_x) and nonlocal terms in the \mathbf{T}_O (\mathbf{Z}_{20}) tendency (from [4]) are indicated in Figs. 9e-f and 10e-f by shading (contours); note that these terms while evaluated at the equator contain effects from all latitudes.

The initial anomaly for the shorter 9-month optimization time has an SST component that is broadly similar to the corresponding SST-LIM optimal initial condition (not shown, but see PS95) except in the central equatorial Pacific where it has half the amplitude, a positive basin-wide thermocline anomaly centered in the east central Pacific similar to that often viewed as an important ENSO precursor (e.g., Wyrski 1985; Jin 1997; Meinen and McPhaden 2000; Clarke and Van Gorder, 2003; McPhaden et al. 2006) and a westerly wind stress anomaly at roughly the same longitude with off-equatorial maxima (Fig. 9a). Optimal SST anomaly amplification over the next nine months is consistent with Bjerknes (1969) feedback: the thermocline term $\mathbf{L}_{TZ}\mathbf{Z}_{20}$ (Fig. 9f, shading) forces rapid amplification of anomalously warm SST in the east Pacific, which in turn (along with the initial SST anomaly) drives intensification and westward expansion of anomalous equatorial westerly wind stress (not shown) that drives (Fig. 9f, contours) the \mathbf{Z}_{20} anomaly to intensify and move eastward (Fig. 9d), and so on. Maximum $\mathbf{L}_{TZ}\mathbf{Z}_{20}$ forcing of SST occurs near the \mathbf{Z}_{20} maximum at about 110°W; a secondary $\mathbf{L}_{TZ}\mathbf{Z}_{20}$ maximum near 140°W might represent advective feedback since it is located near large zonal gradients of both mean SST and anomalous \mathbf{Z}_{20} . Meanwhile, in the west Pacific zonal wind stress forcing $\mathbf{L}_{Zt}\tau_x$ (Fig. 9f) generates a negative \mathbf{Z}_{20} anomaly (Fig. 9d), with minima both north and south of the equator (Fig. 9b) consistent with Ekman pumping from the curl of easterly wind stress anomalies centered at about 15°N and 15°S. The non-local portion of $\mathbf{L}_{ZZ}\mathbf{Z}_{20}$ forcing also enhances the west Pacific \mathbf{Z}_{20} anomaly but is

generally much weaker (Fig. 9e) except near the secondary Z_{20} minimum located around 130°E and 6°N (Fig. 9b). SST forcing by the resulting negative Z_{20} anomaly (via $L_{TZ}Z_{20}$) drives cooler SSTs in the west Pacific (Fig. 9f) but not in the central Pacific where it is offset by the non-local SST term (Fig. 9e, shading). This result is consistent with equatorial SST tendencies during the 1997/98 El Niño just east of the dateline, where negative vertical advection was offset by positive advection by the mean zonal current (Boulanger and Menkes 2001).

Anomalous “equatorial heat content” (as represented by equatorial Z_{20} integrated in the region 2°S-2°N, 120°E-85°W) increases the first two months before decreasing to zero at $t = 9$ months. This increase is consistent with the initial off-equatorial wind stress (e.g., Wang et al. 2003) that also weakens after about two months. Zonal wind stress forcing of Z_{20} in the east Pacific and Z_{20} forcing of SST both peak at $t = 7$ months, at which time zonal wind stress forcing of equatorial heat content also becomes negative. Still, SST anomaly amplification continues for two more months, peaking when the (negative) SST term has grown to balance the thermocline term (e.g., Jin 1997).

Subsequent SST anomaly decay is accelerated when the negative western Pacific thermocline anomaly finally expands eastwards along the equator (Fig. 9d), reaching South America by about $t = 18$ months (Fig. 9c) and causing equatorial SSTs to become cool even as subtropical SSTs remain warm. This eastward movement of negative Z_{20} does not occur, however, until the wind stress forcing (Fig. 9f) has weakened sufficiently to be overcome by the internal ocean dynamics represented by the nonlocal thermocline term (Fig. 9e). In general, wind stress forcing appears to be crucial to the ENSO anomaly decay. For example, in the west Pacific it is less ocean dynamics than wind stress forcing

that drives the negative thermocline anomaly whose eastward propagation ultimately causes the equatorial SST anomaly to strongly decay and even change sign. This is consistent with the suggestion that wind forcing in the west Pacific was of primary importance in initiating the termination of the 1997/98 El Nino (McPhaden 1999; Boulanger and Menkes 2001).

Repeating this integration but first setting the initial \mathbf{Z}_{20} and τ_x anomalies to zero results in similar SST evolution but with peak amplitude reduced by almost half (not shown), demonstrating that the initial thermocline and SST anomalies contribute roughly equally to SST amplification. If the initial conditions shown in Fig. 9a evolve using \mathbf{L}_{noz} instead, the peak anomaly is not only weaker but also more localized and located much closer to the dateline (not shown).

In contrast to $\mathbf{v}_I(9)$, the initial SST portion of $\mathbf{v}_I(18)$ (Fig. 10a) is relatively much stronger than the initial thermocline anomaly. Notably, the southwest Pacific and Indian Ocean SST anomalies persist for several months (e.g., Fig. 10d) while off-equatorial westerly wind stress anomalies rapidly intensify in both hemispheres of the eastern Pacific (Fig. 10b) and deepen the equatorial thermocline there (Figs. 10d and f). [Adding additional τ_x PCs to \mathbf{x} to capture more west Pacific variance does not change this picture.] As the anomaly evolves, it never reaches a stage where it is nearly the same as $\mathbf{v}_I(9)$, with perhaps the closest similarity occurring at about $t = 6$ months primarily for central and eastern Pacific SST (cf. $t = 0$ in Fig. 9d with $t = 6$ months in Fig. 10d). Subsequent anomaly evolution ($t = 6$ -18 months) is only broadly similar to that shown for the 9-

month optimal and moreover extends over a longer period consistent with more persistent wind stress forcing of \mathbf{Z}_{20} (Fig. 10f).

Most of the evolution from $\mathbf{v}_I(18)$ is due to the initial SST, in contrast to $\mathbf{v}_I(9)$; a second integration with the initial \mathbf{Z}_{20} anomaly set to zero reduces peak SST by less than 15% (not shown). However, the *evolution* of \mathbf{Z}_{20} remains essential, since the thermocline term ultimately drives most of the eastern Pacific SST amplification (Fig. 10f). Alternatively, when $\mathbf{v}_I(18)$ is evolved with the \mathbf{L}_{noz} operator, there is very little SST growth.

When considering optimal structures, it is important whether this *potential* growth actually occurs and is observed to be linearly proportional to the projection of the initial anomaly on the leading right singular vectors, as predicted by the LIM. In addition, do the optimal structures shown in Figs. 9 and 10 improve upon those from the SST-LIM; that is, are they more relevant to the observed system? To answer this, following PS95 and others we compared observed anomalies projected on the initial conditions shown in Figs. 9a and 10a to the projection of observed SST anomalies upon the predicted evolved structure 9 (Fig. 9b) and 18 (Fig. 10c) months later, respectively, as shown in Fig. 11a ($\tau = 9$ months) and c ($\tau = 18$ months). This analysis was repeated using the corresponding SST13-LIM optimal structures (not shown); results are shown in Fig. 11b ($\tau = 9$ months) and d ($\tau = 18$ months). The increased linear correlation and reduced scatter about the least squares lines in the panels on the left relative to those on the right indicate that optimal SST growth is better captured by the extended LIM. Of course, some scatter about the least squares line is still expected due to the noise \mathbf{F}_s . The slopes of the dashed lines should correspond to the amplification factors $\lambda_I(\tau)$, and in fact they are quite close. This

also serves as additional evidence that \mathbf{L} is independent of τ_0 , since these calculations have all been made for intervals $\tau \gg \tau_0 = 3$ months.

Stratifying into pre- (blue) and post- (red) 1976/77 periods shows no significant long-term change in the relationship (i.e., change in slope) for the extended LIM. Observed decadal changes in variability could then be represented by random variation of noise forcing projecting differently upon the optimal initial conditions, as opposed to a decadal change in underlying dynamics. Finally, while the 1997/98 El Niño event is somewhat better simulated with the extended LIM than the SST-LIM, it remains an outlier and may represent an event for which we cannot exclude a role for predictable nonlinearity.

5.3 *Eigenmodes contributing to optimal structures*

For the SST-LIM, the leading optimal structure can be well approximated by just three nonnormal eigenmodes of \mathbf{L} (PS95; Penland and Matrosova 2006). We find this too for $\mathbf{v}_I(9)$ and its evolution into $\mathbf{u}_I(9)$, where again all three are propagating eigenmodes (that is, complex conjugate pairs with complex eigenvalues each representing period and e-folding time) with periods of about 4 years ('4-yr eigenmode'; Fig. 12), 1.9 years ('2-yr eigenmode'; Fig. 13), and 21 years ('bidecadal eigenmode'; Fig. 14). [The complete set of 23 eigenmodes $\boldsymbol{\phi}_j$ and corresponding complex eigenvalues σ_j are determined from the eigenanalysis $\mathbf{L}\boldsymbol{\phi}_j = \sigma_j\boldsymbol{\phi}_j$.] The SST components and periods are similar to the corresponding SST-LIM eigenmodes (not shown, but see Penland and Matrosova 2006), but the e-folding times of both the 4-yr and bidecadal eigenmodes are about double those of their SST-LIM counterparts; the 2-yr eigenmode e-folding time is unchanged.

The 4-yr and 2-yr eigenmodes are not orthogonal (with a minimum 40° angle between them) as is evident in their similar structures at the SST minimum (Figs. 12a and 13a) and SST maximum (Figs. 12b and 13b) phases. Consequently, an initial state quite similar to $\mathbf{v}_1(9)$ can be constructed by simply taking the 4-yr eigenmode in a phase about 9 months prior to its SST maximum (Fig. 15a), and then mostly “covering it up” by adding to it the 2-yr eigenmode with amplitude and phase corresponding to Fig. 15b, resulting in the anomaly shown in Fig. 15c (cf. Fig. 9a). [The statistics of the noise determined by (3) show these two eigenmodes tend to be excited together and in opposite phases.] Subsequently, the 2-yr eigenmode undergoes relatively more rapid propagation and decay (Fig. 13c), “revealing” the more slowly evolving 4-yr eigenmode (Fig. 12c) and eventually weakly reinforcing it by $t = 9$ months (Figs. 15d-f). This simple transition from destructive to constructive interference between these two eigenmodes is the basis of optimal growth, with the bidecadal and other eigenmodes playing important but lesser roles.

Some features of the 2-yr and 4-yr eigenmodes appear similar to “recharge/discharge oscillator” (Jin 1997; Burgers et al 2005) and/or “delayed-oscillator” (Schopf and Suarez 1988; Battisti and Hirst 1989) eigenmodes as suggested by theory and found in eigenanalyses based on various linearized versions of the Zebiak and Cane (ZC; 1987) intermediate complexity coupled atmosphere-ocean model (e.g., Jin and Neelin 1993; Dijkstra and Neelin 1999; Fedorov and Philander 2001; An and Jin 2001; MacMynowski and Tziperman 2008; Bejarano and Jin 2008). In both eigenmodes, as they evolve from minimum (panels a) toward maximum (panels b) SST phase, the eastward propagating thermocline anomaly leads and forces SST amplification, while the zonally averaged

equatorial thermocline anomaly decreases from its maximum value to zero, consistent with a “discharge” phase. After the thermocline anomaly reaches the eastern boundary it spreads rapidly northward along the coast to about 14°N (8°N) and then moves westward, curving slightly southward as it crosses the Pacific, consistent with Rossby wave propagation (e.g., Schopf et al. 1981), then back to the equator to seemingly complete the cycle (shown in Figs. 12c and 13c). It is uncertain whether these cyclic signals are important in setting the periods of the modes, or if the tropical dynamics set modal time scales which then select for those subtropical Rossby waves whose corresponding basin-crossing times allow them to be part of the modal structure. A second thermocline extremum in the far west Pacific located much closer to the equator is driven largely by $\mathbf{L}_{ZZ}\mathbf{Z}_{20}$ and could be consistent with equatorial Rossby waves (e.g., Battisti and Hirst 1989). But in general, the wind stress forcing $\mathbf{L}_{Z\tau}\boldsymbol{\tau}_x$ is too important throughout the life cycle of both eigenmodes for the thermocline anomaly evolution to be considered as free Kelvin or Rossby wave propagation, especially near both boundaries. Additionally, the wind stress term drives amplification of the east-west \mathbf{Z}_{20} gradient on the equator, consistent with many earlier studies dating back to Wyrtki. In the subtropics, \mathbf{T}_o and $\boldsymbol{\tau}_x$ both lead the westward moving \mathbf{Z}_{20} anomaly as it passes through about 140°W and are in phase with \mathbf{Z}_{20} west of the dateline (Fig. 12c).

The faster evolution of the 2-yr eigenmode appears related to its different $\boldsymbol{\tau}_x$ and SST structure. Along the equator, $\boldsymbol{\tau}_x$ for the 4-yr eigenmode extends from the dateline through the SST maximum at about 120°W , whereas $\boldsymbol{\tau}_x$ reverses sign for the 2-yr eigenmode at about 140°W , the location of the eigenmode’s more westward SST maximum. SST and

zonal wind stress anomalies also have greater meridional extent, particularly south of the equator, for the slower eigenmode. On the other hand, the two eigenmodes have only minor thermocline differences, primarily of amplitude; in fact, the evolution in Fig. 12 (Fig. 13) is not much altered if the thermocline anomaly from the 2-yr (4-yr) eigenmode is initially replaced with the thermocline anomaly from the corresponding phase of the 4-yr (2-yr) eigenmode (not shown).

Equatorial SST evolution is dominated by thermocline forcing in the 4-yr eigenmode, but for the 2-yr eigenmode the non-local SST term is relatively larger and acts to drive the SST anomaly westward along the equator (Fig. 13c), until near the dateline SST becomes almost exactly out of phase with the thermocline anomaly below and so is weakened (consistent with the overall SST variance sink in Fig. 7c). For both eigenmodes, internal ocean dynamics (i.e., non-local thermocline forcing) drives eastward propagation of the equatorial thermocline anomaly, a process that is reinforced (opposed) by equatorial wind stress forcing thus also contributing to the shorter (longer) time scale of the 2-yr (4-yr) eigenmode.

The bidecadal eigenmode bears some resemblance to “decadal” ENSO variability (e.g., Zhang et al. 1997) and its contribution to $\mathbf{v}_I(9)$ is essential for capturing the decadal tail of the $\mathbf{T}_O/\text{PC1}$ spectrum (Fig. 5). Its much longer time scale is consistent with its more poleward subtropical \mathbf{Z}_{20} anomalies in both hemispheres, which after being induced by anomalies moving from the equator in the east central Pacific propagate more slowly toward the western boundary (Figs. 14c and d) as might be expected of subtropical Rossby waves (Capotondi and Alexander 2001) at these higher latitudes (e.g., Chelton and Schlax 1996). On the other hand, while in the Southern Hemisphere the wind stress

forcing primarily initiates the waves, in the Northern Hemisphere the anomaly appears coupled to the atmosphere. Once near the western boundary, both signals propagate first equatorward and then rapidly eastward to the east central Pacific to complete the loop. However, recall that the bidecadal eigenmode has an e-folding time far shorter than its period and thus it does not actually represent an oscillation (Newman 2007).

For longer optimization periods, the optimal structure projects more strongly upon other eigenmodes besides the three eigenmodes discussed above, although the 4-yr eigenmode remains the largest component. In this case, predictable ENSO evolution over periods of a year and more may not be so clearly identified with a few eigenmodes.

6 Concluding remarks

To better diagnose ocean dynamics and improve forecast skill we have extended the PS95 SST-only LIM to include thermocline depth and zonal wind stress. Over time intervals of several months the extended LIM yields minimal forecast improvement but provides a deeper diagnosis of SST dynamics, suggesting that a central Pacific thermocline anomaly, found as an ENSO precursor by many previous studies, is as important to optimal ENSO initiation as the optimal SST pattern originally found by PS95. Over longer time intervals, however, the extended LIM notably improves upon the SST-only LIM in all measures, including long-lead tropical SST predictions, simulation of power spectra and lag co-variance statistics, and the relevance of leading optimal structures (Fig. 11), giving further support to the effectively linear, stochastically forced view of tropical ocean variability. While some remaining deficiencies of this LIM may represent truly predictable (i.e., slowly-varying) nonlinear internal ocean dynamics capturable only by a high-dimensional fully nonlinear CGCM (Chen et al. 2004), we

might anticipate at least some further improvement by explicit representation of additional oceanic processes within the LIM's state vector, such as vertical stratification, currents, the extratropics, and/or atmospheric variability. It is particularly encouraging that, despite the inherent limitations on ocean data assimilation, the inclusion of \mathbf{Z}_{20} has improved the LIM's representation of ENSO dynamics.

Our results suggest that ENSO is essentially a fairly simple episodic (e.g., Kessler 2002) linear process in which a rapidly evolving eigenmode, driven predominantly but not exclusively by shallow SST-atmosphere dynamics, first destructively and then weakly constructively interferes with a more slowly evolving eigenmode driven by mixed SST/ocean dynamics. Since the damping time scale of the slower mode is about half its period, it continues to predictably evolve for over a quarter cycle; that is, an ENSO episode involves anomaly growth, decay, and overshoot, the latter occurring only along the equator with a weak sign reversal of anomalous SST and zonally-integrated warm water volume. This picture is enriched but not fundamentally altered by the presence of the other eigenmodes. Some previous observational studies have found similar structures in the tropical Pacific with 4- and 2-yr periods (e.g., Jiang et al. 1995; White et al. 2003), although no decay time scale was associated with them. Also, eigenanalysis using the full ZC model (Bejarano and Jin 2008) results in two leading eigenmodes, again with 4-yr and 2-yr periods, that capture many but not all of the gross characteristics noted above. Note that theoretical studies of eigenmodes often focus on the weakly unstable portion of a large parameter space, in which case variations in ENSO (or “flavors”) occur because changes in the background state alter which of the two leading eigenmodes is most unstable (e.g., Fedorov and Philander 2001; Bejarano and Jin 2008). Our results suggest

instead that *both* (stable) eigenmodes are always relevant since ENSO growth is largely due to their modal interference. Hence, events differ because noise projects differently on the entire set of eigenmodes, and background state changes in stability properties may have only minor impact. Note also that the leading optimal structure is the “best-case scenario”; sub-optimal ENSO events are also possible, depending on how noise excites the different eigenmodes.

We also find a second optimal structure allowing for significant SST anomaly growth over time intervals longer than a year, which was not evident in the SST-only LIM. Growth still occurs when initial destructive interference with the 4-yr mode evolves into constructive interference, although this process is now the result of many rather than a few eigenmodes. The initial anomaly for this optimal precursor lies mostly within the SST field, dominated perhaps by remote west Pacific and Indian ocean anomalies, yet subsequent ENSO development cannot be captured by SST alone since it is driven by persistent off-equatorial wind stress in the eastern Pacific that deepens (shallows) the equatorial thermocline to drive warm (cold) SST anomaly amplification (as suggested for example by Wang et al. 2003).

Interestingly, longer time optimal growth does not involve predictable evolution first to the 9-month optimal structure itself and thence to ENSO development. Note that the 9-month optimal’s initial thermocline anomaly might be excited by a series of MJO-like events and/or westerly wind bursts driving downwelling Kelvin waves that deepen the thermocline (e.g., Kessler et al. 1995; McPhaden 1999; Bergman et al. 2001; Zavala-Garay et al. 2005), and extratropical noise could excite the optimal’s initial SST portion, as in the “seasonal footprinting” mechanism (Vimont et al. 2003; Chang et al. 2007).

Also, the comparable importance of both initial SST and thermocline anomalies to subsequent ENSO development is consistent with the idea that a large ENSO event may require both mechanisms as a trigger (e.g., Vimont et al. 2003; Anderson 2007). To the extent these mechanisms act to produce the optimal structure largely through unpredictable noise events, the optimal structure itself would be unpredictable, and thus the predictability of ENSO growth initiated by some combination of these processes alone is limited to about 9-10 months.

“Metrics” of important phenomena within coupled GCMs generally do not directly measure dynamical processes of interest but rather their resulting variability. For example, Nino3 power spectra typically used to compare SST variability due to ENSO (e.g., Guilyardi et al. 2009) do not determine how, only whether, ENSO dynamics differ between models. By constructing even a rudimentary air-SST-ocean LIM, we can go beyond simpler metrics to estimate the relative impact of different feedback terms in the coupled air-sea system, and their importance both within the overall SST variance budget and to the evolution of ENSO events. This can serve as an important baseline against which we can compare coupled dynamics simulated by coupled GCMs. In particular, since the 4-yr and 2-yr eigenmodes together provide a fairly compact representation of observed ENSO dynamics, it may prove useful to compare corresponding eigenmodes determined from the output of coupled GCM runs. Moreover, recall that in the extreme case where thermocline feedbacks are entirely decoupled from the surface in the LIM, SST spectra become more sharply peaked with reduced decadal variability and SST variability is centered more in the central than eastern Pacific. Similarly, Newman et al. (2009) found that removing air-sea coupling in their tropical LIM of weekly averages led

to a greatly weakened ENSO whose period was too short and whose maximum amplitude was too far west. These are all common CGCM failings, suggesting that climate LIMs might also be useful for diagnosing feedbacks leading to errors in comprehensive coupled climate models.

7 Acknowledgements

The authors thank Antonietta Capotondi, Cécile Penland and Amy Solomon for helpful conversations. This work was partially supported by a grant from NOAA CLIVAR-Pacific.

8 References

- Alexander MA, Matrosova L, Penland C, Scott JD, Chang P (2008) Forecasting Pacific SSTs: linear inverse model predictions of the PDO. *J Clim* 21:385–402
- An SI, Jin FF (2001) Collective role of thermocline and zonal advective feedbacks in the ENSO mode. *J Clim* 14:3421–3432
- Anderson BT (2007) Intraseasonal atmospheric variability in the extratropics and its relation to the onset of tropical Pacific sea surface temperature anomalies. *J Clim* 20:926–936
- Battisti DS, Hirst AC (1989) Interannual variability in a tropical atmosphere–ocean model: Influence of the basic state, ocean geometry, and nonlinearity. *J Atmos Sci* 46:1687–1712
- Bejarano L, Jin FF (2008) Coexistence of Equatorial Coupled Modes of ENSO. *J Clim* 21:3051–3067
- Bergman JW, Hendon HH, Weickmann KM (2001) Intraseasonal air–sea interactions at the onset of El Niño. *J Clim* 14:1702–1719
- Bjerknes J (1969) Atmospheric teleconnections from the equatorial Pacific. *Mon Wea Rev* 97:163–172
- Boulanger JP, Menkes C (2001) The Trident Pacific model. Part 2: role of long equatorial wave reflection on sea surface temperature anomalies during the 1993–1998 TOPEX/POSEIDON period. *Clim Dyn* 17:175–186

- Burgers G, van Oldenborgh GJ (2003) On the impact of local feedbacks in the central Pacific on the ENSO cycle. *J Clim* 16:2396-2407
- Burgers G, Jin FF, van Oldenborgh GJ (2005) The simplest ENSO recharge oscillator. *Geophys Res Lett* 32:L13706, doi:10.1029/2005GL022951
- Capotondi A, Alexander MA (2001) Rossby waves in the tropical North Pacific and their role in decadal thermocline variability. *J Phys Oceanogr* 31:3496-351
- Carton JA, Giese BS (2008) A reanalysis of ocean climate using Simple Ocean Data Assimilation (SODA). *Mon Wea Rev* 136:2999-3017
- Chang P, Zhang L, Saravanan R, Vimont DJ, Chiang JCH, Ji L, Seidel H, Tippett MK (2007) Pacific meridional mode and El Niño-Southern Oscillation. *Geophys Res Lett* 34:L16608, doi:10.1029/2007GL030302
- Chelton DB, Schlax MG (1996) Global observations of oceanic Rossby waves. *Science* 272:234-238
- Chelton DB, Wentz FJ, Gentemann CL, de Szoeke RA, Schlax MG (2000) Satellite microwave SST observations of transequatorial tropical instability waves. *Geophys Res Lett* 27:1239-1242
- Chen D, Cane MA, Kaplan A, Zebiak SE, Huang D (2004) Predictability of El Niño over the past 148 years. *Nature* 428:733–736
- Clarke AJ, Van Gorder S (2003) Improving El Niño prediction using a space-time integration of Indo-Pacific winds and equatorial Pacific upper ocean heat content. *Geophys Res Lett* 30:1399, doi:10.1029/2002GL016673

- Dijkstra HA, Neelin JD (1999) Coupled Processes and the Tropical Climatology. Part III: Instabilities of the Fully Coupled Climatology. *J Clim* 12:1630–1643
- Farrell B (1988) Optimal excitation of neutral Rossby waves. *J Atmos Sci* 45:163–172
- Fedorov AV, Philander SG (2001) A Stability Analysis of Tropical Ocean–Atmosphere Interactions: Bridging Measurements and Theory for El Niño. *J Clim* 14:3086–3101
- Fedorov AV, Harper SL, Philander SG, Winter B, Wittenberg A (2003) How Predictable is El Niño? *Bull Amer Meteor Soc* 84:911–919
- Flügel M, Chang P (1996) Impact of dynamical and stochastic processes on the predictability of ENSO. *Geophys Res Lett* 23:2089–2092
- Frankignoul C, Hasselman K (1977) Stochastic climate models. Part II: Application to sea–surface temperature variability and thermocline variability. *Tellus* 29:289–305
- Guilyardi E, Wittenberg A, Fedorov A, Collins M, Wang C, Capotondi A, van Oldenborgh GJ, Stockdale T (2009) Understanding El Niño in Ocean–Atmosphere General Circulation Models: Progress and Challenges. *Bull Amer Meteor Soc* 90:325–340
- Hasselmann K (1976) Stochastic climate models. Part I. Theory. *Tellus* 28:474–485
- Jiang N, Neelin JD, Ghil M (1995) Quasi-quadrennial and quasi-biennial variability in the equatorial Pacific, *Clim Dyn* x, pp-pp
- Jin FF (1997) An Equatorial Ocean Recharge Paradigm for ENSO. Part I: Conceptual Model. *J Atmos Sci* 54:811–829

- Jin FF, An SI (1999) Thermocline and zonal advective feedbacks within the equatorial ocean recharge oscillator model for ENSO. *Geophys Res Lett* 26:2989-2992
- Jin FF, Kim ST, Bejarano L (2006) A coupled-stability index for ENSO. *Geophys Res Lett* 33:L23708, doi:10.1029/2006GL027221
- Jin FF, Neelin JD (1993) Modes of interannual tropical ocean-atmosphere interaction—a unified view. Part III: Analytical results in fully coupled cases. *J Atmos Sci* 50:3523-3540
- Jochum M, Cronin MF, Kessler WS, Shea D (2007) Observed horizontal temperature advection by tropical instability waves. *Geophys Res Lett* 34:L09604, doi:10.1029/2007GL029416
- Johnson SD, Battisti DS, Sarachik ES (2000) Empirically Derived Markov Models and Prediction of Tropical Pacific Sea Surface Temperature Anomalies. *J Clim* 13:3–17
- Kalnay E, et al (1996) The NCEP/NCAR 40-Year Reanalysis Project. *Bull Amer Meteor Soc* 77:437–471
- Kang IS, An SI, Jin FF (2001) A Systematic Approximation of the SST Anomaly Equation for ENSO. *J Met Soc Japan*, 79, 1-10
- Kessler WS (2002) Is ENSO a cycle or a series of events? *Geophys Res Lett* 29:2125, doi:10.1029/2002GL015924
- Kessler WS, McPhaden MJ (1995) The 1991-93 El Niño in the central Pacific. *Deep-Sea Res II* 42:295-334
- Kessler WS, McPhaden MJ, Weickmann KM (1995) Forcing of intraseasonal Kelvin waves in the equatorial Pacific. *J Geophys Res* 100(C6)10,613–10,631

- Latif M, Graham NE (1992) How much predictive skill is contained in the thermal structure of an OGCM? *J Phys Oceanogr* 22:951-962
- MacMynowski DG, Tziperman E (2008) Factors Affecting ENSO's Period. *J Atmos Sci* 65:1570–1586
- McPhaden MJ (1999) Genesis and evolution of the 1997-98 El Niño. *Science* 283:950-954
- McPhaden MJ, Zhang X, Hendon HH, Wheeler MC (2006) Large scale dynamics and MJO forcing of ENSO variability. *Geophys Res Lett* 33:L16702, doi:10.1029/2006GL026786
- Meinen CS, McPhaden MJ (2000) Observations of Warm Water Volume Changes in the Equatorial Pacific and their Relationship to El Niño and La Niña. *J Clim* 13:3551-3559
- Moore A, Kleeman R (1997) The singular vectors of a coupled-atmosphere model of ENSO. II: Sensitivity studies and dynamical interpretation. *Quart J Roy Meteor Soc* 123:983–1006
- Moore A, Kleeman R (1999) The non-normal nature of El Niño and intraseasonal variability. *J Clim* 12:2965-2982
- Neelin JD (1991) The slow sea surface temperature mode and the fast-wave limit: Analytic theory for tropical interannual oscillations and experiments in hybrid coupled models. *J Atmos Sci* 48:584-606
- Neelin JD, Jin FF (1993) Modes of interannual tropical ocean-atmosphere interaction—a unified view. Part II: Analytical results in the weak-coupling limit. *J Atmos Sci* 50:3504-3522

- Neelin JD, Battisti DS, Hirst AC, Jin FF, Wakata Y, Yamagata T, Zebiak SE (1998) ENSO theory. *J Geophys Res* 103:14261-14290
- Newman M, Sardeshmukh PD, Winkler CR, Whitaker JS (2003) A study of subseasonal predictability. *Mon Wea Rev* 131:1715-1732
- Newman M (2007) Interannual to decadal predictability of tropical and North Pacific sea surface temperatures. *J Clim* 20:2333-2356
- Newman M, Sardeshmukh PD (2008) Tropical and stratospheric influences on extratropical short-term climate variability. *J Clim* 21:4326-4347
- Newman M, Sardeshmukh PD, Penland C (2009) How important is air-sea coupling in ENSO and MJO evolution? *J Clim* 22:2958-2977
- Papanicolaou G, Kohle W (1974) Asymptotic theory of mixing stochastic ordinary differential equations. *Commun Pure Appl Math* 27:641-668
- Penland C (1989) Random forcing and forecasting using principal oscillation pattern analysis. *Mon Wea Rev* 117:2165—2185
- Penland C (1996) A stochastic model of IndoPacific sea surface temperature anomalies. *Physica D* 98:534--558
- Penland C, Flügel M, Chang P (2000) Identification of Dynamical Regimes in an Intermediate Coupled Ocean–Atmosphere Model. *J Clim* 13:2105–2115
- Penland C, Ghil M (1993) Forecasting Northern Hemisphere 700-mb geopotential heights using principal oscillation patterns. *Mon Wea Rev* 121:2355—2372
- Penland C, Matrosova L (1994) A balance condition for stochastic numerical models with application to the El Niño-Southern Oscillation. *J Clim* 7:1352-1372

- Penland C, Matrosova L (2006) Studies of El Niño and interdecadal variability in Tropical sea surface temperatures using a nonnormal filter. *J Clim* 19:5796-5815
- Penland C, Sardeshmukh PD (1995) The optimal growth of tropical sea surface temperature anomalies. *J Clim* 8:1999–2024
- Picaut J, Ioualalen M, Menkes C, Delcroix T, McPhaden MJ (1996) Mechanism of the Zonal Displacements of the Pacific Warm Pool: Implications for ENSO. *Science* 274:1486-1489
- Rayner NA, Parker DE, Horton EB, Folland CK, Alexander LV, Rowell DP, Kent EC, Kaplan A (2003) Global analyses of sea surface temperature, sea ice, and night marine air temperature since the late nineteenth century. *J Geophys Res* 108:4407, doi:10.1029/2002JD002670
- Schopf PS, Anderson DLT, Smith R (1981) Beta-dispersion of low frequency Rossby waves. *Dynamics of Atmospheres and Oceans* 5:187-214
- Schopf PS, Suarez MJ (1988) Vacillations in a coupled ocean–atmosphere model. *J Atmos Sci* 45:549–566
- Thompson CJ, Battisti DS (2001) A linear stochastic dynamical model of ENSO. Part II: Analysis. *J Clim* 14:445-466
- Vimont DJ, Wallace JM, Battisti DS (2003) The seasonal footprinting mechanism in the Pacific: Implications for ENSO. *J Clim* 16:2668–2675
- Wang W, McPhaden MJ (2000) The surface-layer heat balance in the equatorial Pacific ocean. Part II: Interannual variability. *J Phys Ocean* 30:2989-3008

- Wang X, Jin FF, Wang Y (2003) A tropical ocean recharge mechanism for climate variability. Part I: Equatorial heat content changes induced by the off-equatorial wind. *J Clim* 16:3585-3598
- White WB, Tourre YM, Barlow M, Dettinger M (2003) A delayed action oscillator shared by biennial, interannual, and decadal signals in the Pacific Basin. *Geophys Res* 108:doi:10.1029/2002JC001490
- Winkler CR, Newman M, Sardeshmukh PD (2001) A linear model of wintertime low-frequency variability. Part I: Formulation and forecast skill. *J Clim* 14:4474-4494
- Wyrtki K (1985) Water displacements in the Pacific and the genesis of El Niño cycles. *J Geophys Res*: 90, 7129-7132
- Xue Y, Leetmaa A, Ji M (2000) ENSO Prediction with Markov Models: The Impact of Sea Level. *J Clim* 13:849–871
- Zavala-Garay J, Zhang C, Moore AM, Kleeman R (2005) The linear response of ENSO to the Madden–Julian Oscillation. *J Clim* 18:2441–2459
- Zebiak SE, Cane MA (1987) A model El Niño-southern oscillation. *Mon Wea Rev* 115:2268-78
- Zelle H, Appeldoorn G, Burgers G, van Oldenborgh GJ (2004) The relationship between sea surface temperature and thermocline depth in the eastern equatorial Pacific. *J Phys Ocean* 34:643-655
- Zhang Y, Wallace JM, Battisti DS (1997) ENSO-like interdecadal variability. *J Clim* 10:1004–1020

9 Figures

Figure 1: Variance (contours) and fraction of local variance explained by EOF truncation (color shading) for variables used in the LIM. Top: SST (T_O); contour interval 0.25 K^2 . 2nd row: 20°C isotherm depth (Z_{20}); contour interval 125 m^2 . Bottom row: zonal wind stress (τ_x); contour interval.

Figure 2. Cross-validated forecast skill (1959-2000) of T_O for forecast leads of 9 and 18 months, for the LIM (top), the SST13-LIM (middle), and the LIM using initial T_O and τ_x conditions only (i.e., all forecasts are initialized with $Z_{20}(t=0)=0$).

Figure 3. Cross-validated forecast skill (1959-2000) of Niño3.4, defined as the area averaged SST in the region 5S-5N, 170W-120W, for the LIM (black) the LIM using initial T_O and τ_x conditions only (i.e., all forecasts are initialized with $Z_{20}(t=0)=0$; thin black line), the SST13-LIM (blue), and the SST23-LIM (green).

Figure 4. Observed (top panels), LIM (middle panels) and SST13-LIM (bottom panels) T_O lag-covariance. (left) 9-month lag-covariance; (center) 18-month lag-covariance; (right) 36-month lag-covariance. Note that the observed lag-covariances are the based on the full (that is, not truncated in the EOF basis) gridded anomaly fields. Contour interval is 0.04 K^2 .

Figure 5. Power spectra for the three leading SST (T_O) PCs (red lines), compared to that predicted by the LIM (blue lines). Gray shading represents the 95% confidence interval determined from a 1000-member ensemble of 42 yr LIM model runs (see text for further

details). The green lines indicate spectra generated by \mathbf{L}_{noz} (i.e., $\mathbf{L}_{\text{TZ}}=\mathbf{L}_{\text{ZI}}=0$). In these log(frequency) versus power times angular frequency (ω) plots, the area under any portion of the curve is equal to the variance within that frequency band. Note that displaying power times frequency slightly shifts the power spectral density peak centered at a period of 4.5 years to a variance peak centered at a period of 3.5 years. Insets in each panel show the corresponding EOF and the variance explained by that pattern.

Figure 6. Same as Fig. 5 but for the three leading 20°C isotherm depth (\mathbf{Z}_{20}) PCs.

Figure 7. The local variance budget for SST (see text for description of terms). Panels in the left column are the “non-local” terms and panels in the right column are the “local” terms. Note that the sum of all the panels is equivalent to the noise variance, which is less than one contour level almost everywhere. Contour and shading interval is $0.04 \text{ K}^2\text{month}^{-1}$; positive values are red/yellow and negative values are blue, with the zero contour removed for clarity.

Figure 8. a) Comparison of Maximum Amplification (MA) curves, defined as $[\lambda_1(\tau)]^2$ determined by the SVD of $\mathbf{G}(\tau)$ under the L2 norm of \mathbf{T}_O , for the LIM and the SST-LIMs. b) Pattern correlation of $\mathbf{v}_I(9)$ with $\mathbf{v}_I(\tau)$ for the extended LIM and the SST-LIMs.

Figure 9. Evolution of the optimal initial condition for amplification of SST anomalies in the LIM over a 9-month interval. a) Initial state, and the evolved states b) 9 and c) 18 months later. d) Time-longitude cross-section of the LIM evolution averaged between 2°S-2°N. \mathbf{T}_O is indicated by shading (contour interval 0.175 K), \mathbf{Z}_{20} by contours (contour interval 6 m), and τ_x by blue vectors (scaled by the reference vector 0.02 Nm^{-2} , with

values below 0.002 Nm^{-2} removed for clarity). e and f) Time-longitude cross-section of selected forcing terms in the tendency equations for \mathbf{T}_O (shading; interval 0.05 K/month) and \mathbf{Z}_{20} (contours; interval 0.5 m/month): e) Nonlocal terms; f) \mathbf{Z}_{20} forcing of \mathbf{T}_O tendency and τ_x forcing of \mathbf{Z}_{20} tendency. Note that sign in all panels is arbitrary, but that black contours and red shading are of one sign, and pink contours and blue shading are the other sign. Amplitudes are also arbitrary, but are scaled by a single factor here to have representative values. Note that \mathbf{T}_O is doubled in panel (a) to be more visible.

Figure 10. Same as Fig. 9 but for the evolution of the optimal initial condition for amplification of SST anomalies in the LIM over an 18-month interval.

Figure 11. Projection of observations upon the optimal initial condition for amplification of SST anomalies in the LIM over a 9-month interval, versus the optimal evolved SST state 9 months later, in (a) the extended LIM and (b) the SST13-LIM. Projection of observations upon the optimal initial condition for amplification of SST anomalies in the LIM over a 18-month interval, versus the optimal evolved SST state 18 months later, in (c) the extended LIM and (d) the SST13-LIM. The dashed lines in all four panels represent the expected evolution, with slopes $\lambda_1(\tau)$. Blue circles represent the 1959-1976 period, and red circles the 1977-2000 period. Red dots represent the 1997-98 El Niño event.

Figure 12. The third least damped eigenmode of \mathbf{L} , with period of 4.0 yrs and e-folding time of 2.1 yrs. a) Minimum and b) Maximum SST phases, defined from the root-mean-squared domain SST anomaly. c) Time-space cross-section of the eigenmode evolution, starting from the phase shown in Fig. 15a, along the transect indicated by panel d. \mathbf{T}_O is

indicated by shading (contour interval 0.175 K), \mathbf{Z}_{20} by contours (contour interval 6 m), and τ_x by blue vectors (scaled by the reference vector 0.02 Nm⁻²). Note that sign in all panels is arbitrary, but that black contours and red shading are of one sign, and pink contours and blue shading are the other sign. Amplitudes are also arbitrary, but are scaled by a single factor here to have representative values.

Figure 13. The eighth least damped eigenmode of \mathbf{L} with period of 1.9 yrs and e-folding time of 0.65 yrs. a) Minimum and b) Maximum SST phases, defined from the root-mean-squared domain SST anomaly. c) Time-space cross-section of the eigenmode evolution, starting from the phase shown in Fig. 15b, along the transect indicated by panel d. Plotting conventions as in Fig. 12 except all values in Fig. 13c are scaled by a factor of 3; note that the transect points here are at the same longitudes as the transect points in Fig. 12.

Figure 14. The second least damped eigenmode of \mathbf{L} , with period of 21 yrs and e-folding time of 2.2 yrs. Plotting conventions as in Fig. 12, except that panel c) shows the time-longitude cross-section of the LIM evolution, with exponential decay term removed, at 14°N and d) shows the time-longitude cross-section of the LIM evolution, with exponential decay term removed, at 18°S.

Figure 15. Evolution of the 4-yr and 2-yr eigenmode components of $\mathbf{v}_I(9)$. a) 4-yr eigenmode component at $t = 0$. b) 2-yr eigenmode component at $t = 0$. c) 4-yr plus 2-yr eigenmode components at $t = 0$. d) 4-yr eigenmode component at $t = 9$. e) 2-yr eigenmode component at $t = 9$. f) 4-yr plus 2-yr eigenmode components at $t = 9$. Plotting conventions as in Fig. 9.

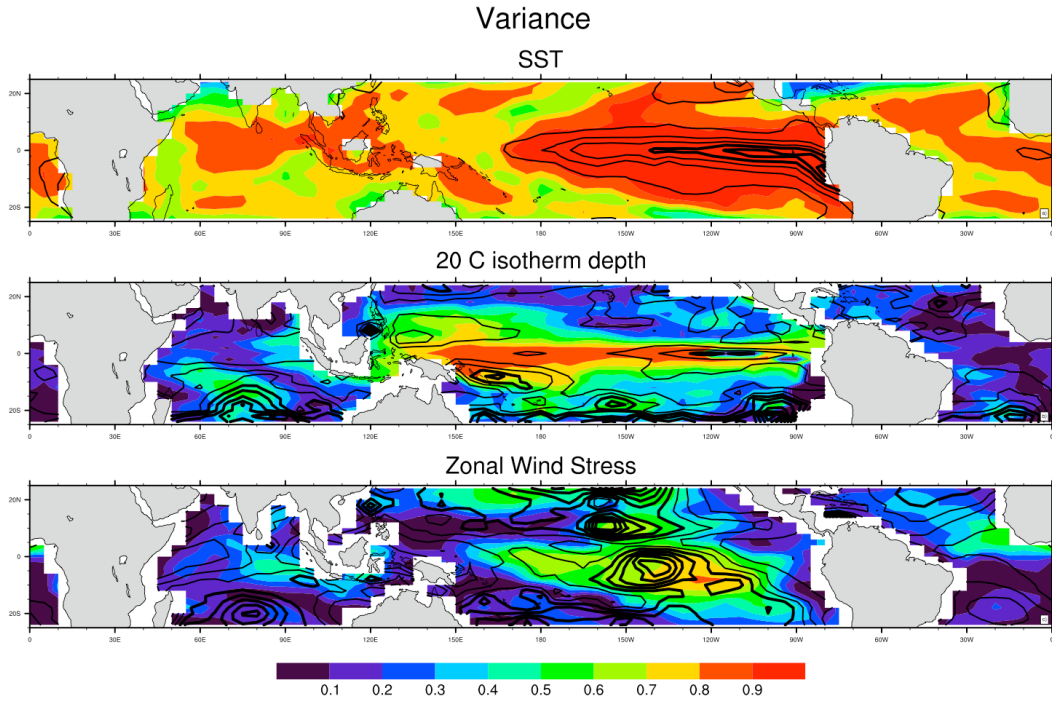


Figure 1: Variance (contours) and fraction of local variance explained by EOF truncation (color shading) for variables used in the LIM. Top: SST (T_o); contour interval 0.25 K^2 . 2nd row: 20°C isotherm depth (Z_{20}); contour interval 125 m^2 . Bottom row: zonal wind stress (τ_x); contour interval $5 \times 10^{-5} \text{ N}^2 \text{ m}^{-4}$.

Anomaly correlation skill of SST forecasts

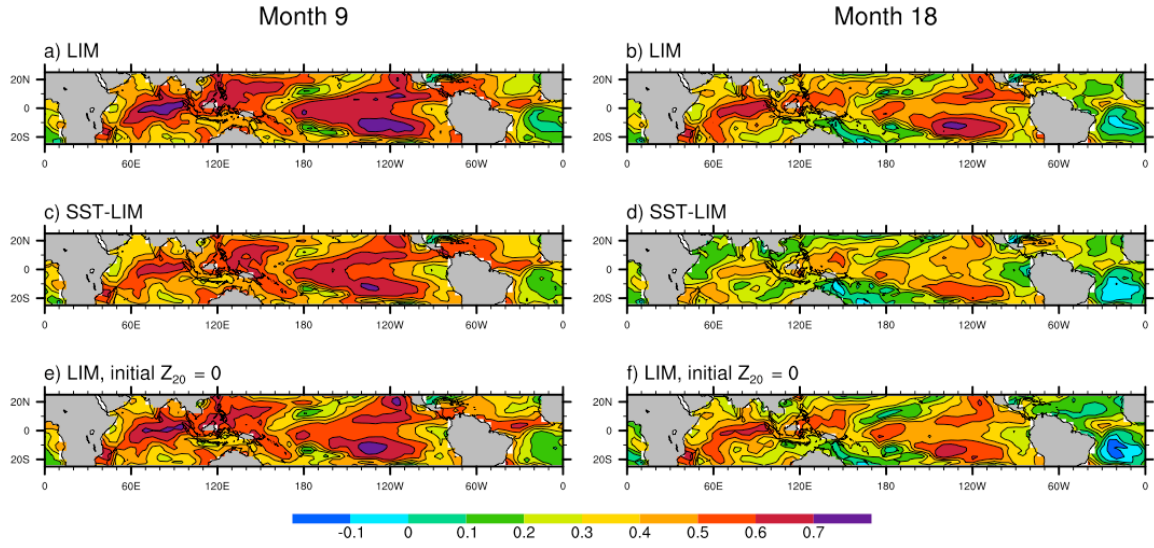


Figure 2. Cross-validated forecast skill (1959-2000) of T_O for forecast leads of 9 and 18 months, for the LIM (top), the SST13-LIM (middle), and the LIM using initial T_O and τ_x conditions only (i.e., all forecasts are initialized with $Z_{20}(t=0)=0$).

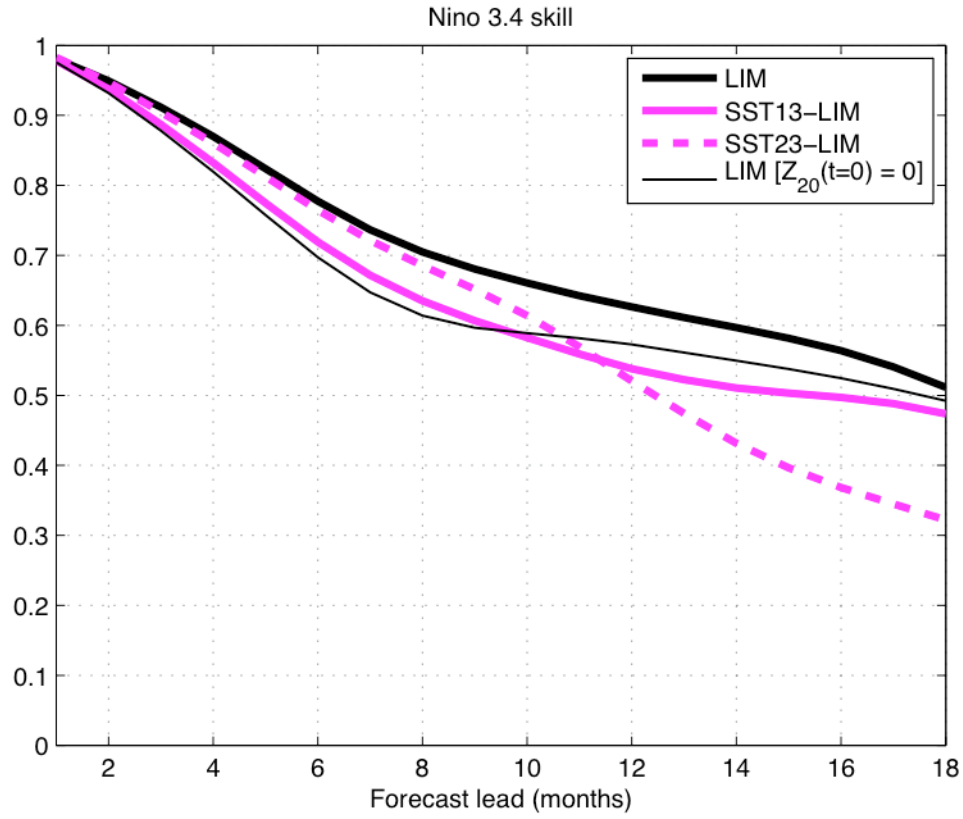


Figure 3. Cross-validated forecast skill (1959-2000) of Niño3.4, defined as the area averaged SST in the region 5S-5N, 170W-120W, for the LIM (black), the LIM using initial \mathbf{T}_0 and $\boldsymbol{\tau}_x$ conditions only (i.e., all forecasts are initialized with $\mathbf{Z}_{20}(t=0)=0$; thin black line), the SST13-LIM (magenta), and the SST23-LIM (dashed magenta).

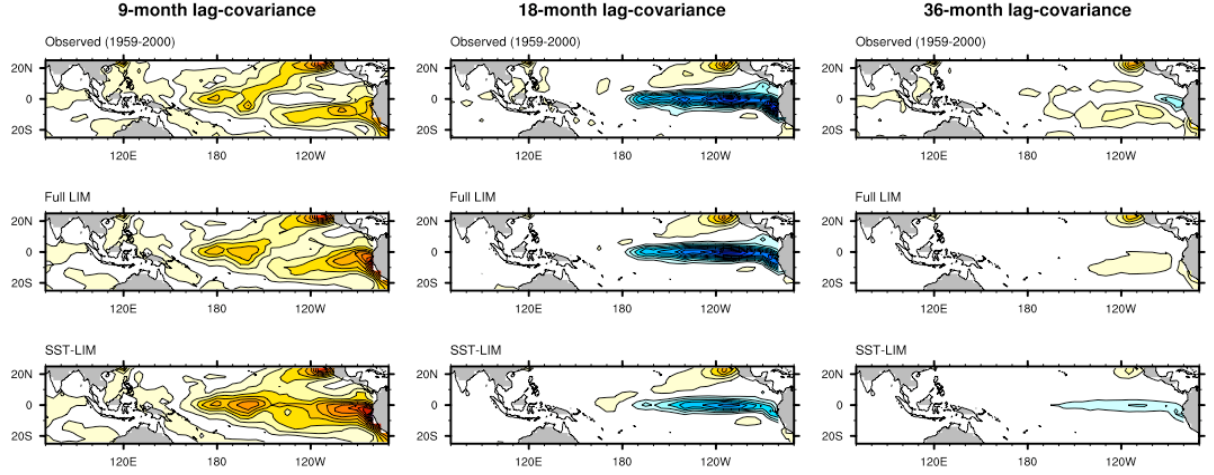


Figure 4. Observed (top panels), LIM (middle panels) and SST13-LIM (bottom panels) T_O lag-covariance. (left) 9-month lag-covariance; (center) 18-month lag-covariance; (right) 36-month lag-covariance. Note that the observed lag-covariances are the based on the full (that is, not truncated in the EOF basis) gridded anomaly fields. Contour interval is 0.04 K^2 .

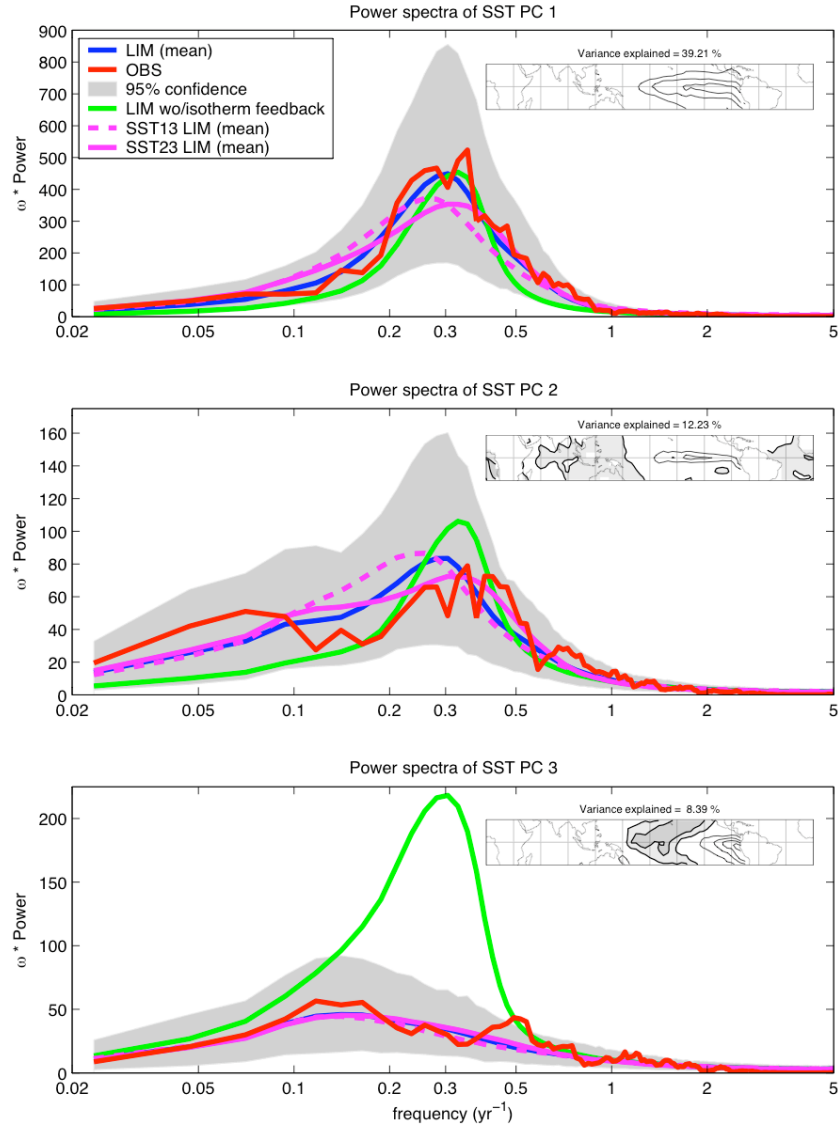


Figure 5. Power spectra for the three leading SST (T_o) PCs (red lines), compared to that predicted by the LIM (blue lines). Gray shading represents the 95% confidence interval determined from a 1000-member ensemble of 42 yr LIM model runs (see text for further details). The green lines indicate spectra generated by L_{noz} (i.e., $L_{\text{TZ}}=L_{\text{ZT}}=0$). In these $\log(\text{frequency})$ versus power times angular frequency (ω) plots, the area under any portion of the curve is equal to the variance within that frequency band. Note that displaying power times frequency slightly shifts the power spectral density peak centered at a period of 4.5 years to a variance peak centered at a period of 3.5 years. Insets in each panel show the corresponding EOF and the variance explained by that pattern.

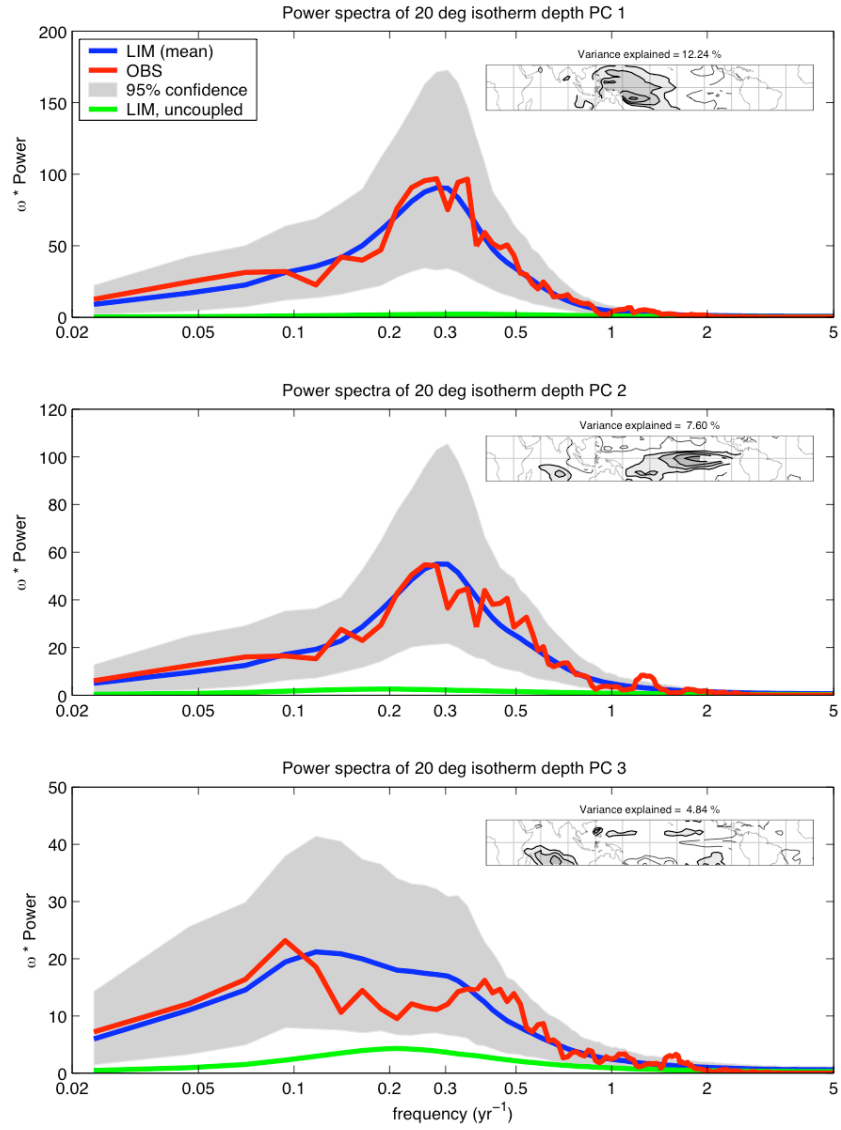


Figure 6. Same as Fig. 5 but for the three leading 20°C isotherm depth (Z_{20}) PCs.

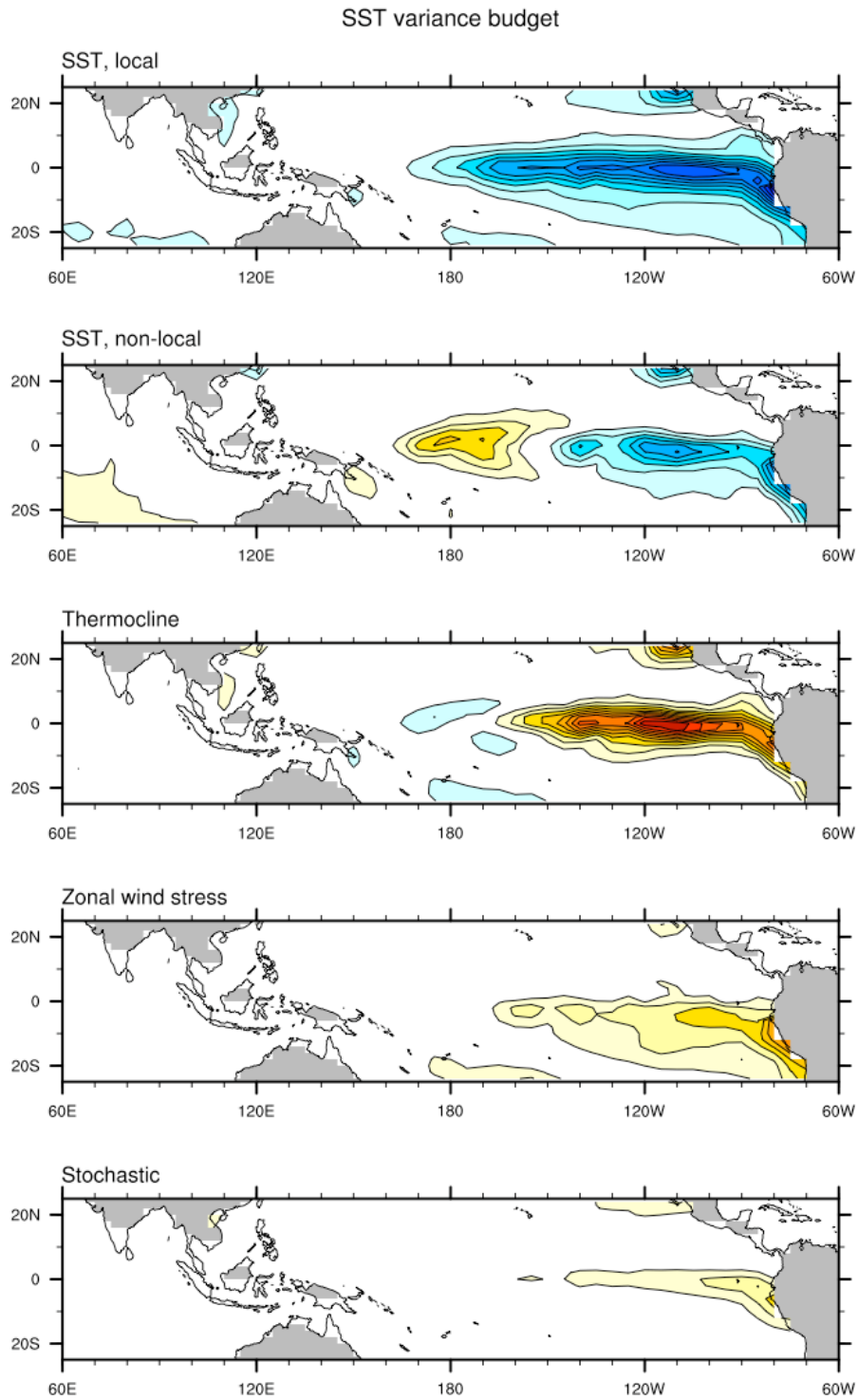


Figure 7. The local variance budget for SST (see text for description of terms). Note that all five panels sum to zero. Contour interval is $0.04 \text{ K}^2 \text{ month}^{-1}$; positive values are red/yellow and negative values are blue, with the zero contour removed for clarity.

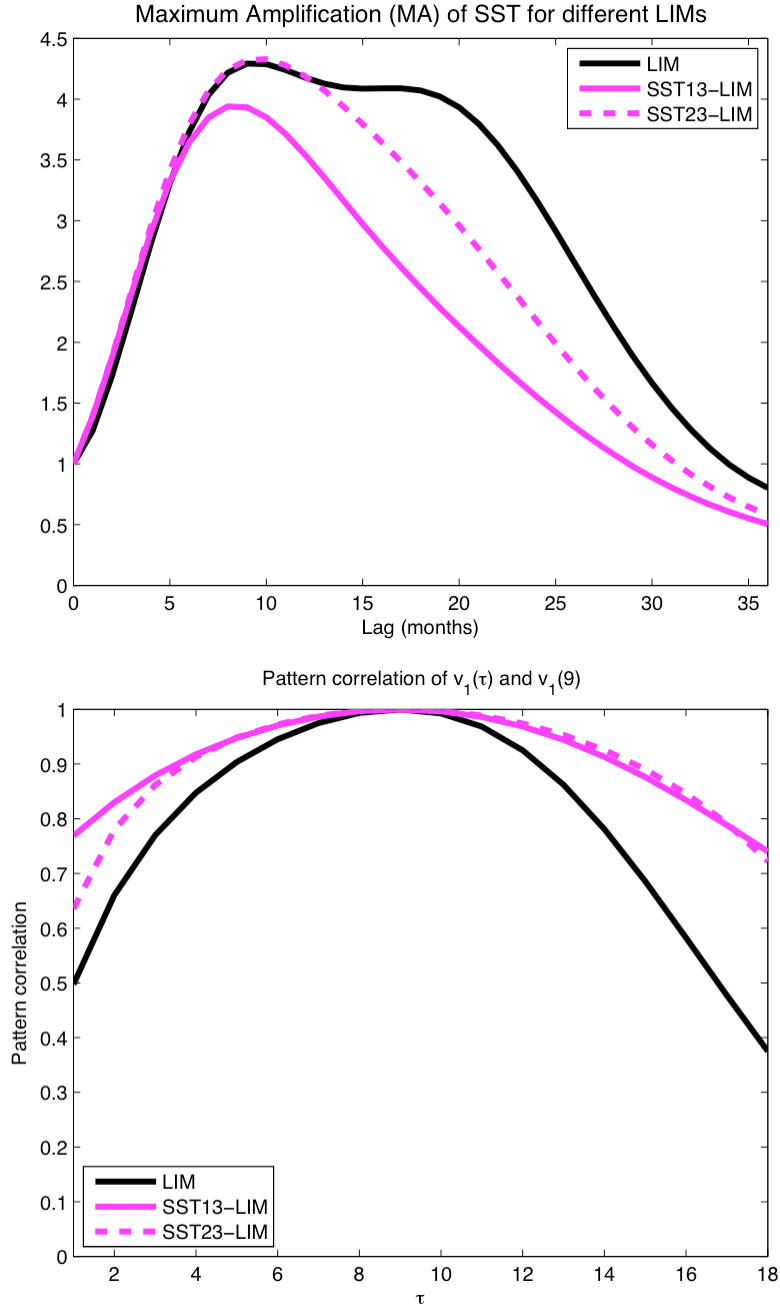


Figure 8. a) Comparison of Maximum Amplification (MA) curves, defined as $[\lambda_1(\tau)]^2$ determined by the SVD of $G(\tau)$ under the L2 norm of T_O , for the extended LIM and the SST-LIMs. b) Pattern correlation of $v_1(9)$ with $v_1(\tau)$ for the extended LIM and the SST-LIMs.

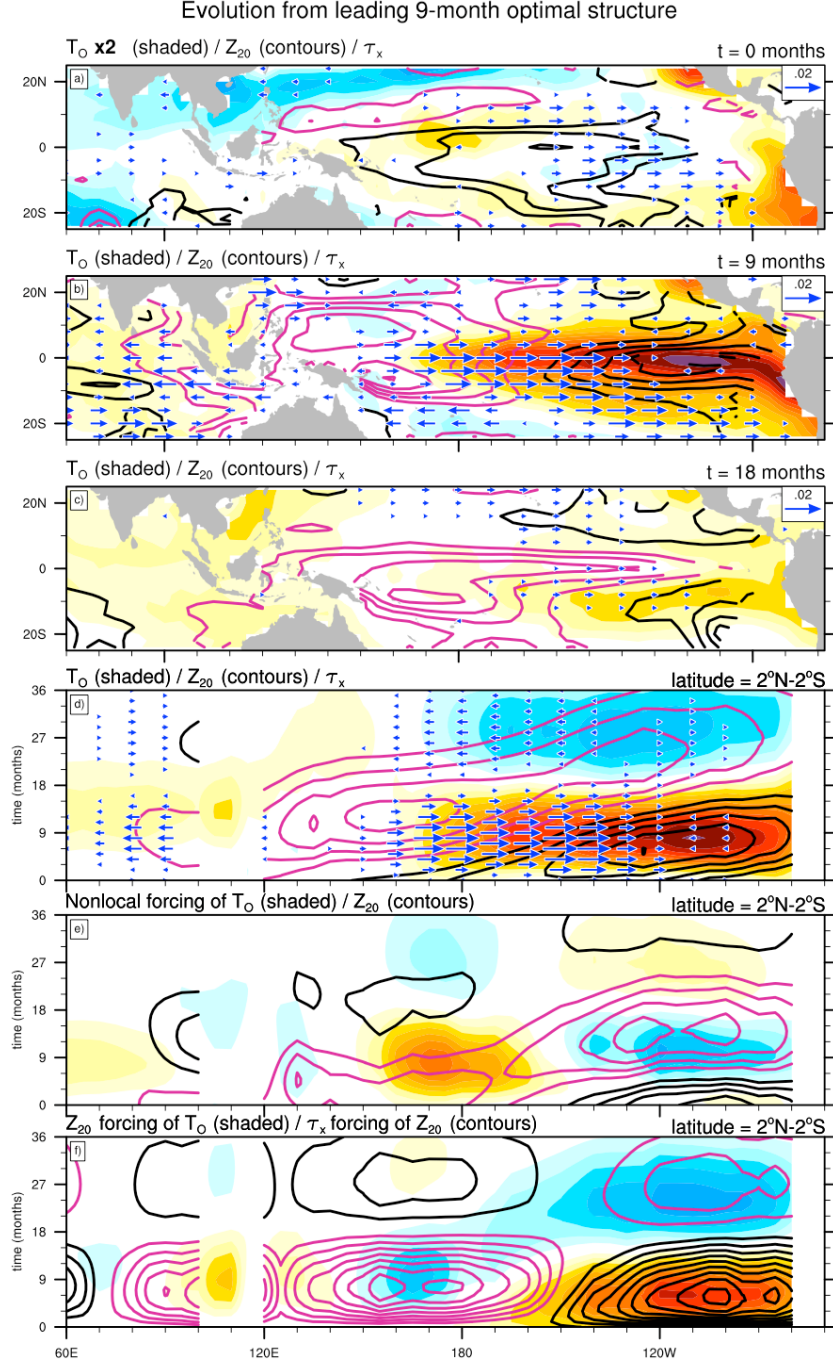


Figure 9. Evolution of the optimal initial condition for amplification of SST anomalies in the LIM over a 9-month interval. a) Initial state, and the evolved states b) 9 and c) 18 months later. d) Time-longitude cross-section of the LIM evolution averaged between 2°S-2°N. T_O is indicated by shading (contour interval 0.175 K), Z_{20} by contours (contour interval 6 m), and τ_x by blue vectors (scaled by the reference vector 0.02 Nm^{-2} , with values below 0.002 Nm^{-2} removed for clarity). e and f) Time-longitude cross-section of selected forcing terms in the tendency equations for T_O (shading; interval 0.05 K/month) and Z_{20} (contours; interval 0.5 m/month): e) Nonlocal terms; f) Z_{20} forcing of T_O tendency and τ_x forcing of Z_{20} tendency. Note that sign in all panels is arbitrary, but that black contours and red shading are of one sign, and pink contours and blue shading are the other sign. Amplitudes are also arbitrary, but are scaled by a single factor here to have representative values. Note that T_O is doubled in panel (a) to be more visible.

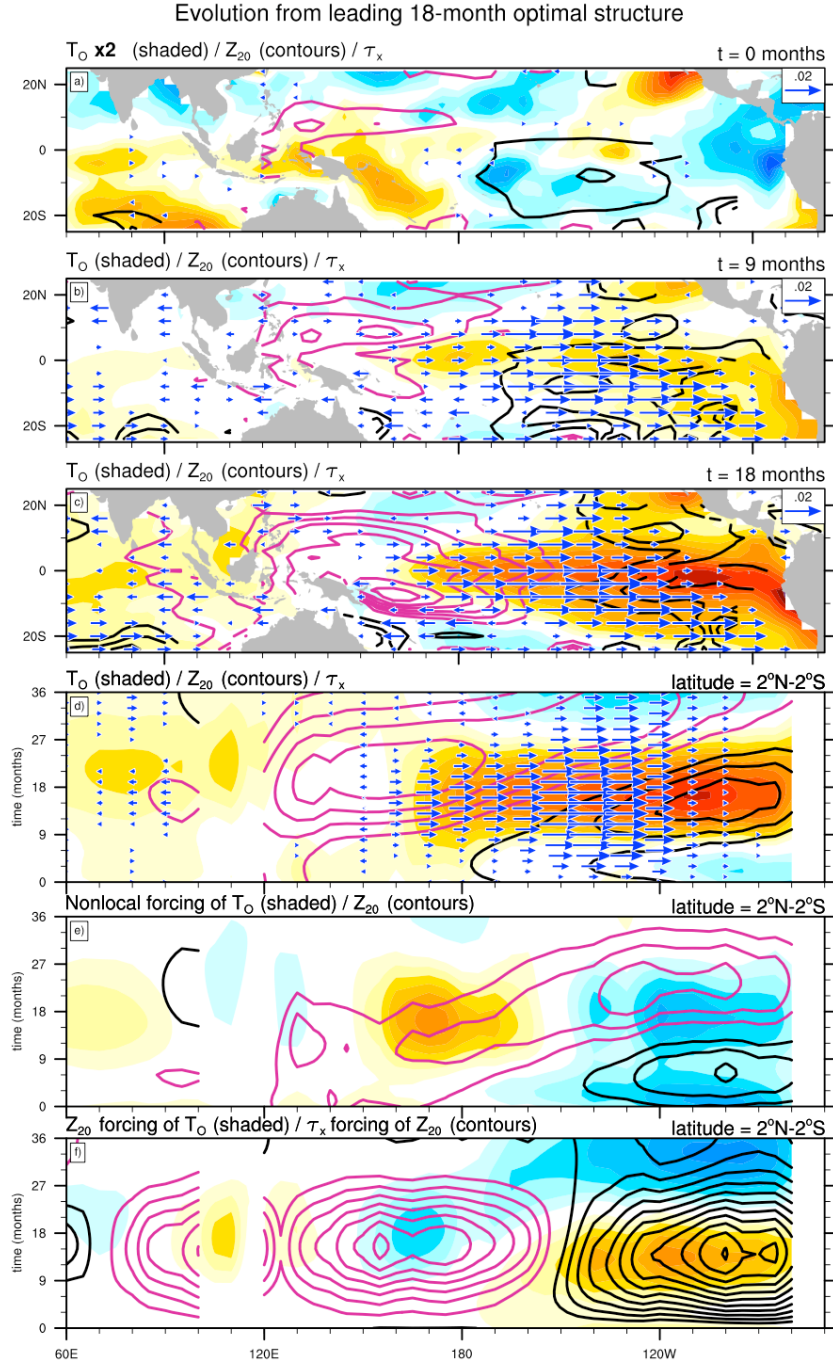


Figure 10. Same as Fig. 9 but for the evolution of the optimal initial condition for amplification of SST anomalies in the LIM over an 18-month interval.

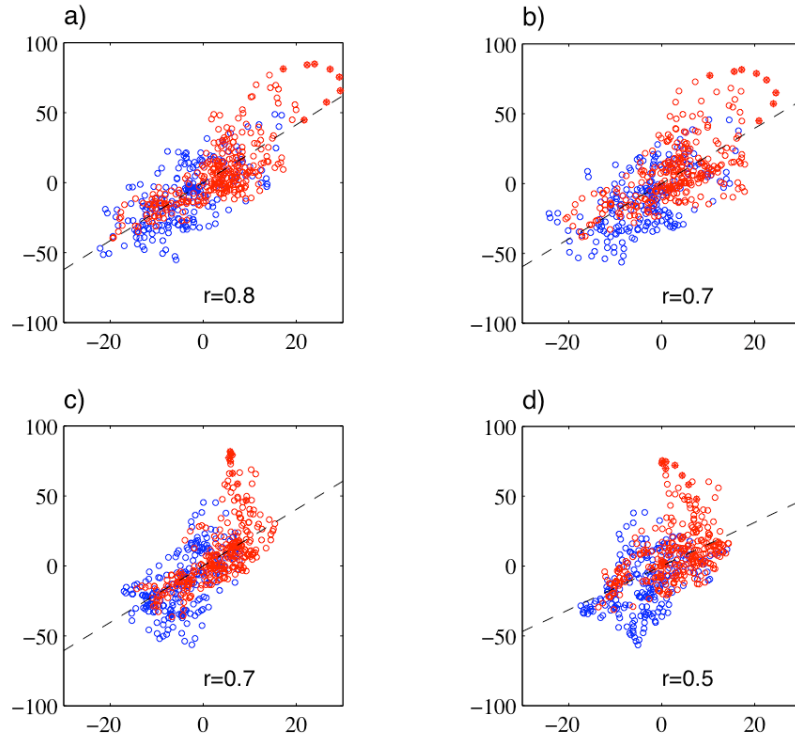


Figure 11. Projection of observations upon the optimal initial condition for amplification of SST anomalies in the LIM over a 9-month interval, versus the optimal evolved SST state 9 months later, in (a) the extended LIM and (b) the SST13-LIM. Projection of observations upon the optimal initial condition for amplification of SST anomalies in the LIM over a 18-month interval, versus the optimal evolved SST state 18 months later, in (c) the extended LIM and (d) the SST13-LIM. The dashed lines in all four panels represent the expected evolution, with slopes $\lambda_1(\tau)$. Blue circles represent the 1959-1976 period, and red circles the 1977-2000 period. Red dots represent the 1997-98 El Niño event.

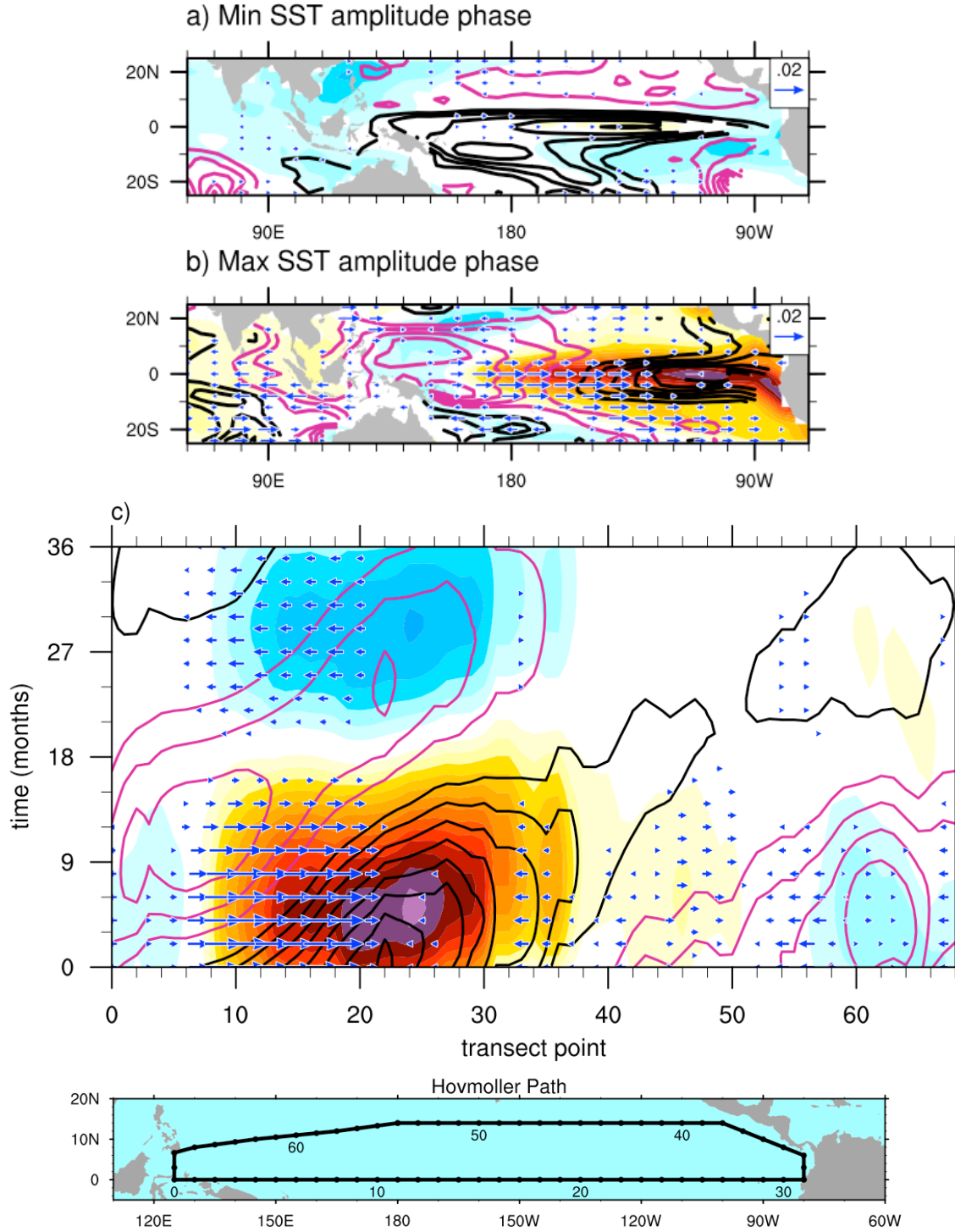


Figure 12. The third least damped eigenmode of \mathbf{L} , with period of 4.0 yrs and e-folding time of 2.1 yrs. a) Minimum and b) Maximum SST phases, defined from the root-mean-squared domain SST anomaly. c) Time-space cross-section of the eigenmode evolution, starting from the phase shown in Fig. 15a, along the transect indicated by panel d. T_O is indicated by shading (contour interval 0.175 K), Z_{20} by contours (contour interval 6 m), and τ_x by blue vectors (scaled by the reference vector 0.02 Nm^{-2}). Note that sign in all panels is arbitrary, but that black contours and red shading are of one sign, and pink contours and blue shading are the other sign. Amplitudes are also arbitrary, but are scaled by a single factor here to have representative values.

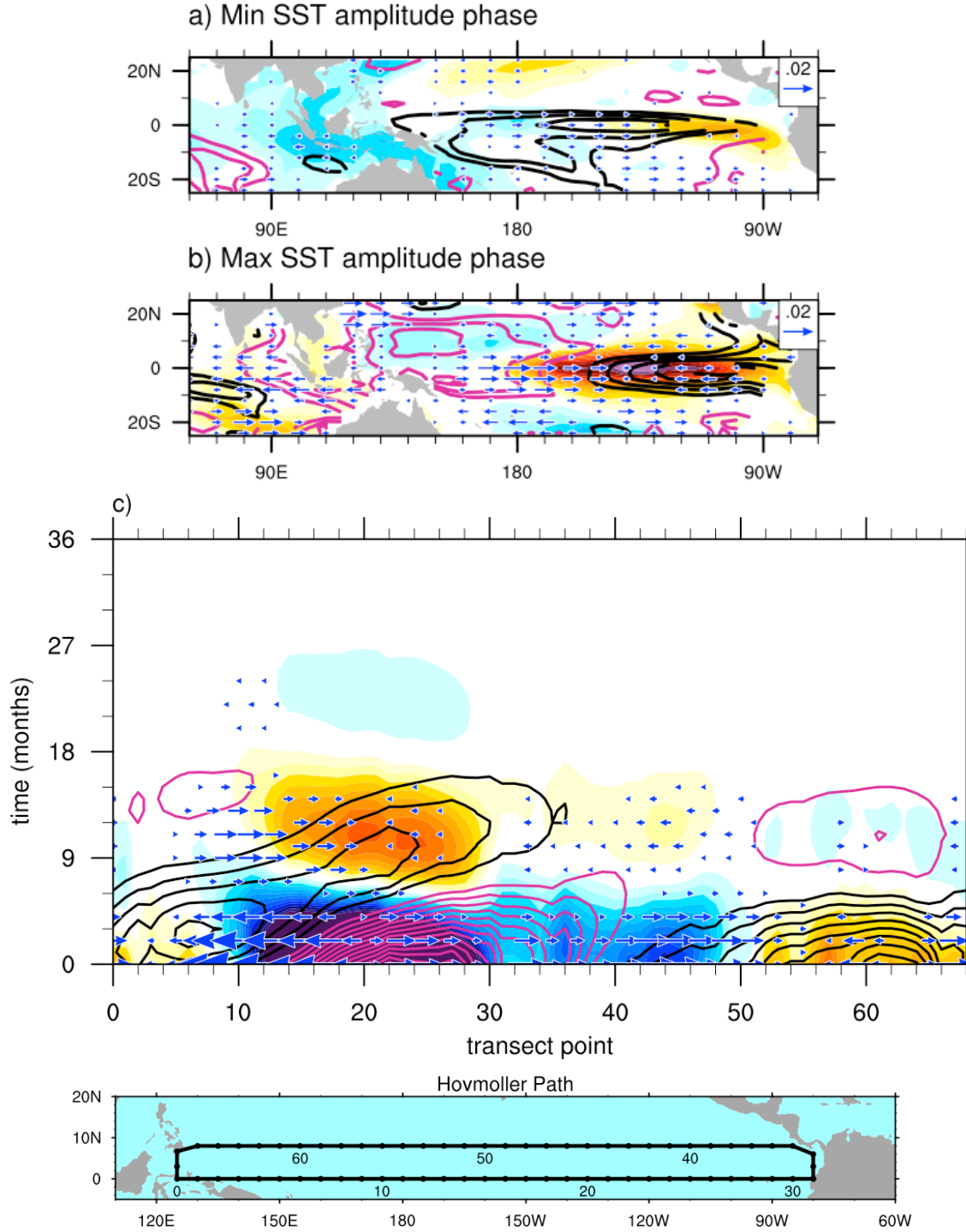


Figure 13. The eighth least damped eigenmode of \mathbf{L} with period of 1.9 yrs and e-folding time of 0.65 yrs. a) Minimum and b) Maximum SST phases, defined from the root-mean-squared domain SST anomaly. c) Time-space cross-section of the eigenmode evolution, starting from the phase shown in Fig. 15b, along the transect indicated by panel d). Plotting conventions as in Fig. 12 except all values in Fig. 13c are scaled by a factor of 3; note that the transect points here are at the same longitudes as the transect points in Fig. 12.

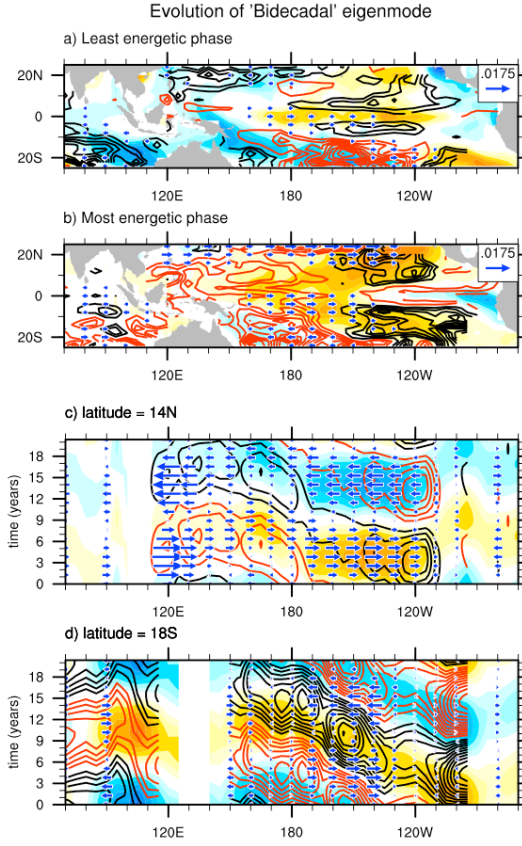


Figure 14. The second least damped eigenmode of \mathbf{L} , with period of 21 yrs and e-folding time of 2.2 yrs. Plotting conventions as in Fig. 12, except that panel c) shows the time-longitude cross-section of the LIM evolution, with exponential decay term removed, at 14°N and d) shows the time-longitude cross-section of the LIM evolution, with exponential decay term removed, at 18°S .

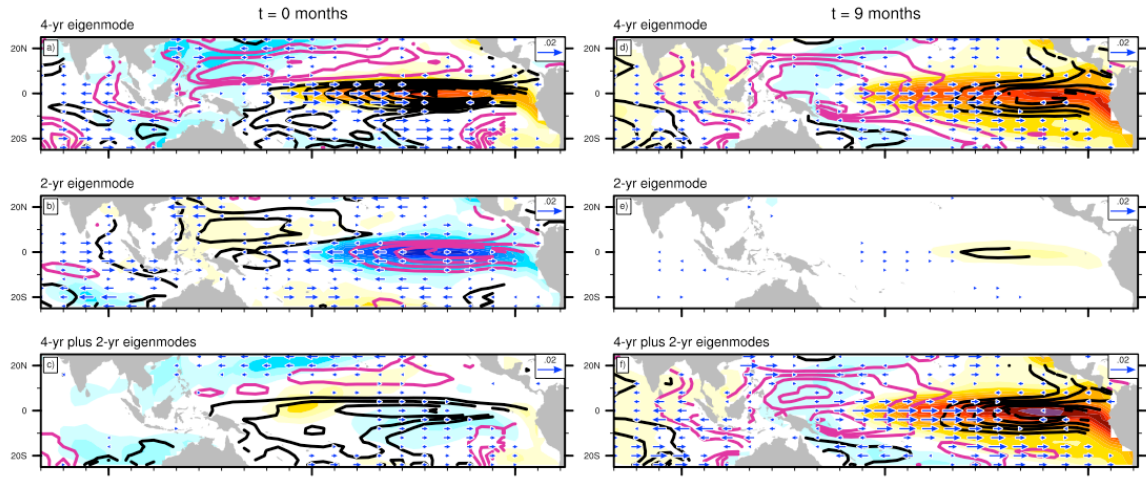


Figure 15. Evolution of the 4-yr and 2-yr eigenmode components of $\mathbf{v}_l(9)$. a) 4-yr eigenmode component at $t = 0$. b) 2-yr eigenmode component at $t = 0$. c) 4-yr plus 2-yr eigenmode components at $t = 0$. d) 4-yr eigenmode component at $t = 9$. e) 2-yr eigenmode component at $t = 9$. f) 4-yr plus 2-yr eigenmode components at $t = 9$. Plotting conventions as in Fig. 9.